STRUCTURAL BIOLOGY

Cell-penetrating Alphabody protein scaffolds for intracellular drug targeting

Erwin Pannecoucke[1,2]*, Maaike Van Trimpont[3,4]*, Johan Desmet[5], Tim Pieters[3,4], Lindy Reunes[3,4], Lisa Demoen[3,4], Marnik Vuylsteke[6], Stefan Loverix[5], Karen Vandenbroucke[5], Philippe Alard[5], Paula Henderikx[5], Sabrina Deroo[5], Franky Baatz[5], Eric Lorent[5], Sophie Thiolloy[5], Klaartje Somers[5†], Yvonne McGrath[5], Pieter Van Vlierberghe[3,4], Ignace Lasters[5‡], Savvas N. Savvides[1,2‡]

The therapeutic scope of antibody and nonantibody protein scaffolds is still prohibitively limited against intracellular drug targets. Here, we demonstrate that the Alphabody scaffold can be engineered into a cell-penetrating protein antagonist against induced myeloid leukemia cell differentiation protein MCL-1, an intracellular target in cancer, by grafting the critical B-cell lymphoma 2 homology 3 helix of MCL-1 onto the Alphabody and tagging the scaffold's termini with designed cell-penetration polypeptides. Introduction of an albumin-binding moiety extended the serum half-life of the engineered Alphabody to therapeutically relevant levels, and administration thereof in mouse tumor xenografts based on myeloma cell lines reduced tumor burden. Crystal structures of such a designed Alphabody in complex with MCL-1 and serum albumin provided the structural blueprint of the applied design principles. Collectively, we provide proof of concept for the use of Alphabodies against intracellular disease mediators, which, to date, have remained in the realm of small-molecule therapeutics.

INTRODUCTION

Monoclonal antibodies are currently at the forefront of clinical treatments for various cancers, infections, and (auto)immune diseases and represent 7 of the top 10 best-selling drugs worldwide in 2018 (*1*, *2*). Although therapeutic monoclonal antibodies are endowed by many favorable characteristics that are important for their use as therapeutic agents, such as long serum half-life, high specificity, and immunological effector functions, they are also critically limited by low tissue penetration and inability to directly address intracellular drug targets. In addition, they impose high production or formulation costs due to low stability and the need for essential posttranslational modifications and harbor complexities in drug administration and patient care. To overcome some of these impediments, alternative approaches emerged, including engineered antibody fragments, such as the recently Food and Drug Administration–approved caplacizumab (*3*), as well as nonantibody protein scaffolds (*4*, *5*). Interest in non-immunoglobulin (Ig) protein scaffolds has been particularly intense because of the ease of screening and selection of high-affinity binders, exquisite stability, scalability, and low cost of production. However, despite successes in preclinical studies, the progression of nonantibody scaffolds to clinical development is often hampered by the limited serum half-life of these small-sized protein scaffolds and, similar to antibodies, their inability to reach intracellular targets (*4*–*6*).

In this study, we sought to develop the Alphabody as a non-Ig protein scaffold that may help to address these challenges in drug discovery and development. Alphabodies are based on a single-chain non-Ig protein scaffold featuring an antiparallel triple-helix coiled-coil fold (Fig. 1A) (*7*). The three helices are each composed of four heptad repeats with tightly packed isoleucines at core positions (*a* and *d*) in a regular "knobs-into-holes" configuration. This all-Ile core endows the Alphabody with exceptional thermal stability (T_M of about 120°C), while allowing for up to 25–amino acid positions that can be varied for the purpose of constructing a binding site to the intended molecular target (*7*). Previously, we developed Alphabodies that act as potent antagonists of the proinflammatory cytokine interleukin-23 (IL-23) (*7*, *8*), an extracellular protein target of clinical importance (*8*, *9*). Here, we engineered Alphabodies to target an intracellular tumorigenic protein, induced myeloid leukemia cell differentiation protein (MCL-1). MCL-1 is a member of the antiapoptotic B-cell lymphoma 2 (BCL-2) family, a group of intracellular antiapoptotic proteins that contain up to four BCL-2 homology (BH) regions. All members of this family are characterized by their antagonism of apoptosis-initiating proteins, such as the pore-forming proapoptotic BCL-2 family members BAK and BAX (*10*–*12*). Under normal conditions, programmed cell death is counteracted by antiapoptotic proteins, such as MCL-1 and BCL-2. However, upon cellular stress, the proapoptotic BH3-only proteins are up-regulated and bind to proapoptotic BCL-2 family members by docking of the BH3-only domain into a hydrophobic groove at the surface of the BCL-2 family member (*13*, *14*). This interaction results in activation of BAK and BAX that will initiate the programmed cell death cascade by permeabilization of the mitochondrial outer membrane.

Many tumors prevent apoptosis by the up-regulation of the antiapoptotic protein MCL-1, which makes it an attractive candidate for anticancer therapy (*15*–*21*). Flavopiridol, a pan-cyclin–dependent kinase inhibitor, and AZD-4573, a selective cyclin-dependent kinase 9 inhibitor, have been developed to indirectly down-regulate MCL-1. In addition, chemotherapeutics such as anthracyclines are known to repress *MCL-1* transcription, but all are associated with

[1]VIB Center for Inflammation Research, 9052 Ghent, Belgium. [2]Unit for Structural Biology, Department of Biochemistry and Microbiology, Ghent University, 9052 Ghent, Belgium. [3]Department of Biomolecular Medicine, Ghent University, Ghent, Belgium. [4]Cancer Research Institute Ghent (CRIG), Ghent, Belgium. [5]Complix N.V., 9052 Ghent, Belgium. [6]Gnomixx, 9090 Melle, Belgium.
*These authors contributed equally to this work.
†Present address: Children's Cancer Institute, Lowy Cancer Research Centre, UNSW Sydney, P.O. Box 81, Randwick, NSW 2031, Australia; School of Women's and Children's Health, UNSW Sydney, Randwick, NSW 2052, Australia.
‡Corresponding author. Email: ignace.lasters@complix.com (I.L.); savvas.savvides@ugent.be (S.N.S.)

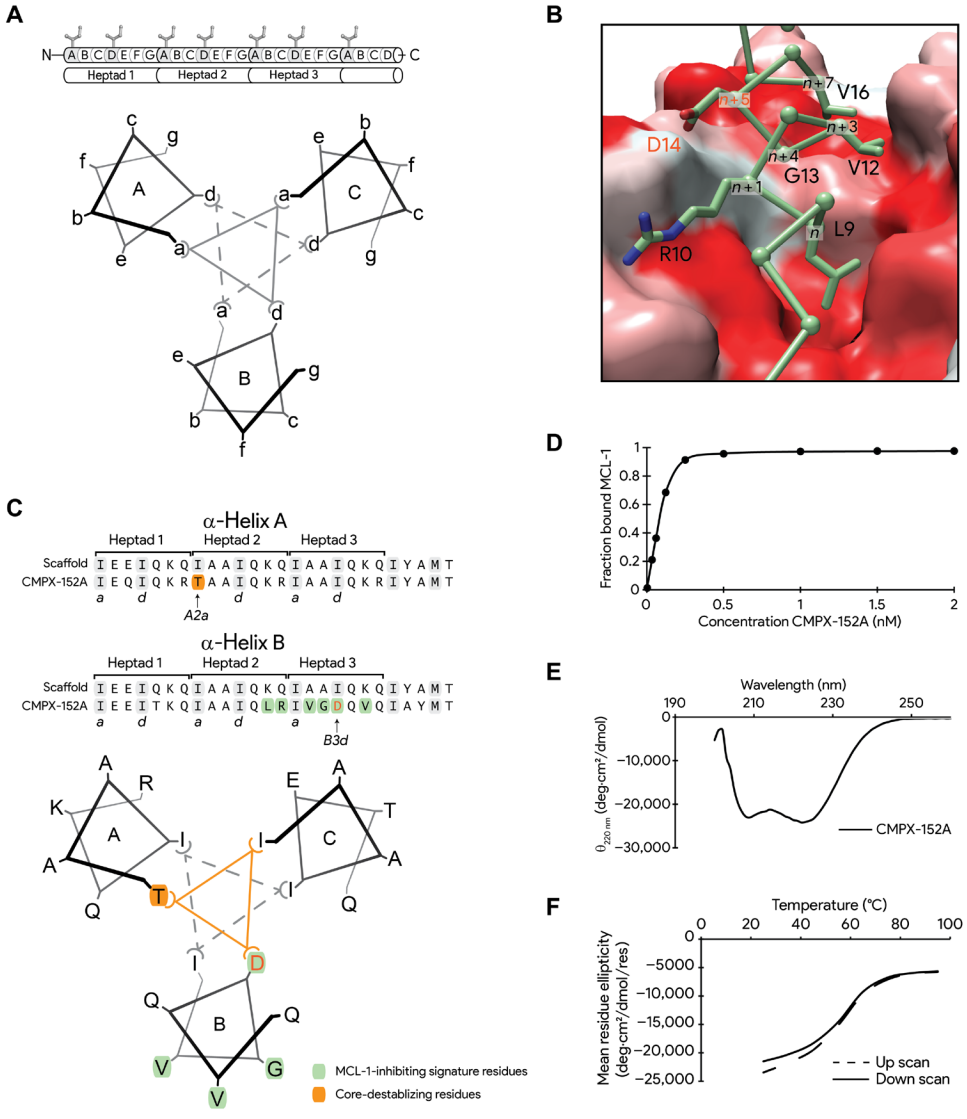

Fig. 1. Grafting of the MCL-1–inhibiting motif onto the Alphabody scaffold. (**A**) Overview of the Alphabody scaffold. Alphabodies are antiparallel triple-helix coiled coils consisting of four heptad repeats in each of the three helical elements. Hydrophobic core interactions between isoleucines at positions *a* and *d* of each heptad stabilize the fold and result in an extremely high thermal stability and other favorable physicochemical parameters (*7*). Top: Linear representation of one helix. Bottom: Cross-sectional helical wheel representation of the interaction between core positions in the coiled coil. Positions within a triangle at the interface of the three helices belong to the same core layer. (**B**) Six residues (stick representation) describe the MCL-1 (surface representation, red is more hydrophobic)–binding motif to the BH3-binding groove. Figure was generated using Protein Data Bank (PDB) code 3MK8. (**C**) Incorporation of the MCL-1 inhibitory footprint onto the Alphabody scaffold required a polar core layer. Top: Six MCL-1 key binding residues (green background) were grafted onto helix B of CMPX-152A, which inserted Asp^{n+5} (orange) into the all-Ile Alphabody core on position *d* of the third heptad of helix B (*B3d*, indicated). To maintain structural stability of CMPX-152A, the Ile at position *a* of the second heptad of helix A (*A2a*, indicated) was substituted for a threonine (orange background). Bottom: Schematic cross section of CMPX-152A showing the Asp^{B3d}-containing core layer. Modeling revealed that the most stable conformation of an Alphabody clusters Thr^{A2a} and Asp^{B3d} into the same core layer (orange triangle). (**D**) Determination by solution enzyme-linked immunosorbent assay (ELISA) of the 8 pM affinity of Alphabody CMPX-152A for MCL-1 ($n = 23$) (*84*). (**E**) Secondary structure characterization in CMPX-152A by circular dichroism revealing an all α-helical content ($n = 1$). (**F**) Representative T_M determination experiment of CMPX-152A by circular dichroism thermal denaturation experiments. T_M value was calculated as the average T_M value of the up and down scan.

considerable side effects limiting their therapeutic potential (*22*–*30*). So far, none of the more than 20 compounds evaluated in preclinical studies or clinical trials have resulted in the approval of an MCL-1–targeted therapy, despite its clear correlation with therapy resistance in various cancers (*20*, *21*, *31*).

In the present study, we report the de novo design of a cell-penetrating Alphabody (CPAB) able to bind to intracellular MCL-1 with high affinity to achieve inhibition. First, we grafted the MCL-1–inhibiting BH3 helix onto the Alphabody template, an endeavor requiring the application of negative design principles facilitated by the high stability of the generic Alphabody scaffold. Next, we designed and optimized cell penetration tags allowing efficient cellular uptake without affecting target binding properties. Last, we extended the serum half-life of this MCL-1–targeting Alphabody by grafting a minimal

albumin-binding moiety to its remaining variable positions. The resulting Alphabody, named CMPX-383B, demonstrates the high level of protein engineering tolerated by the Alphabody scaffold and sets the stage for the use of Alphabodies in disrupting intracellular protein-protein interactions.

RESULTS

Alphabody CMPX-152A integrates the MCL-1 BH3 binding principles into a designed protein scaffold

The Alphabody protein scaffold consists of a contiguous polypeptide that folds into a three-helix coiled coil with antiparallel helix topology, and its entire scaffold surface can be deployed to generate a binding surface for a given target (Fig. 1A) (*7*). To explore the potential of the Alphabody platform for tailored binding to intracellular targets, we sought to neutralize MCL-1, a member of the antiapoptotic BCL-2 family and a clinically validated drug target. It has previously been described that the BH3 helix of MCL-1, when expressed as a standalone molecular entity, becomes a high-affinity inhibitor of MCL-1 (*14*). We hypothesized that MCL-1–interacting residues could be engrafted onto one of the Alphabody α helices to yield a designed Alphabody that can bind to MCL-1 with high affinity and specificity. On the basis of the available complexes of MCL-1 and different inhibitory peptides (table S1), we selected six residues that were hypothesized to play a key role in the specific binding to MCL-1 (Fig. 1B). Together, these residues were positioned to form an amphipathic helical element with hydrophobic residues (Leu^{n}, Val^{n+3}, and Val^{n+7}) on one face and Arg^{n+1}/Asp^{n+5} projecting a polar helical face. In addition, Gly^{n+4} was identified as a key determinant for MCL-1 binding, as any residue with a side chain larger than that of alanine would likely sterically impede MCL-1 binding.

We engrafted these six amino acids onto the B helix of the Alphabody scaffold to yield Alphabody CMPX-152A as a prototype. In silico docking experiments revealed that incorporation of the MCL-1 inhibitory footprint into the Alphabody template required grafting of the $Val^{n+3}Gly^{n+4}Asp^{n+5}$ sequence on heptad positions *bcd* (Fig. 1C, green background, and fig. S1). However, this resulted in the insertion of a negatively charged aspartate residue into the hydrophobic all-isoleucine core of the Alphabody, which would be expected to compromise the stability of the Alphabody. In the absence of options to engineer interactions that electrostatically stabilize this so-called "Asp in core," we applied a negative design methodology that, per design, averted the Alphabody from adopting undesired conformations, such as possible oligomeric species or aggregates (*32*, *33*). To do so, we further destabilized the Asp^{B3d}-containing core layer (Fig. 1C, orange triangle) by substituting Ile^{A2a} by a threonine (Fig. 1C, orange background). The rationale for choosing a threonine residue for this purpose was twofold. First, the amphipathic nature of this residue would allow both a polar interaction with the core aspartate (Fig. 1C, orange triangle) mediated by its hydroxyl group, while its hydrophobic methyl group would be able to interface with the adjacent all-isoleucine core layer (Fig. 1C, gray triangle). Second, threonine is the only naturally occurring amino acid that combines a polar group with an isoleucine-like C_β-branched configuration, which was considered advantageous for replacing an Ile in the Alphabody core. Although the energetic penalty of the Asp in core would be worsened by this additional polar residue in the Alphabody core, in silico modeling revealed that conformations that do not cluster Asp^{B3d} and Thr^{A2a} into the same core layer (Fig. 1C, orange triangle) would be even more unstable and thus more unlikely to form. Hence, we actively engineered against any other conformation than the desired one.

The resulting Alphabody CMPX-152A showed ultrahigh affinity for MCL-1, with a K_D = 8 pM (Fig. 1D). This low-picomolar affinity proved to be maintained throughout next generations of Alphabodies (table S2) and could be orthogonally confirmed for the last generation. Circular dichroism measurements confirmed that CMPX-152A contained the expected amount of helical secondary structure, yet, as expected, the destabilization of a core layer in its fold induced a substantial reduction in thermal stability as compared to the Alphabody template [T_M of 58° and 120°C, respectively, in the presence of 1 M guanidine hydrochloride (GuHCl)] (Fig. 1, E and F) (*7*). However, with a higher than 90% reversible thermal stability in the presence of a chaotrope (table S3), CMPX-152A is more thermostable than the average mesostable protein (T_M of 54°C in the absence of GuHCl) (*34*).

Reformatting of anti–MCL-1 Alphabodies to enable cell penetration and intracellular protein inhibition

Given the intracellular localization of MCL-1, we developed a second generation of MCL-1 inhibitory Alphabodies that can be taken up by cells, thereby setting the stage for addressing a fundamental challenge in the targeting of intracellular drug targets by protein therapeutics. The mechanism of how particular sequences endow peptides with cell-penetrating capacities is still under debate. Nevertheless, it has been recognized that naturally occurring cell-penetrating sequences, such as TAT, penetratin, and the synthetic peptide cFΦR4, mediate cell penetration by the presentation of guanidium groups to the negatively charged phospholipid bilayer (*35*–*40*). We leveraged these insights to develop reformatted Alphabodies that can translocate across the cell membrane without compromising their target binding properties. The developed CPAB tag consists of seven consecutive arginine-proline repeats ($[RP]_7$) that were engineered to be added cotranslationally at the N and C terminus of the Alphabody polypeptide (Fig. 2A). The rationale for the choice of a proline residue flanked by arginines was twofold. On the basis of currently known cell-penetrating peptides, we inferred that a proline residue would increase uptake by reducing the electrostatic repulsion between the protein backbone amides and the lipid bilayer. Furthermore, the hydrophobic nature of a proline residue was expected to enhance the efficiency of cell penetration.

Alphabody CMPX-321A carrying CPAB tags at its N and C terminus (Fig. 2A) was found to efficiently cross the mammalian cell membrane (Fig. 2, B and C). Specifically, we evaluated this newly acquired property by incubating NCI-H929 cells with CMPX-321A, followed by probing their cytosolic content for the presence of the Alphabody using antibodies recognizing the B helix of CMPX-321A (Fig. 2B). After a 2-hour incubation with 2 μM added Alphabody, the detected signal for CMPX-321A in the cytosolic compartment (Fig. 2B, last lane, and fig. S2) exceeded the intensity of the 10-pmol reference (Fig. 2B, second lane), implying a cytosolic concentration of at least 17 μM. The CPAB cellular uptake was further confirmed by immunofluorescence in HeLa cells that were treated for 30 min with CMPX-321A, followed by detection of this Alphabody using an anti-V5 antibody (Fig. 2C, green color). This observation is in contrast to previous experiments, in which no signal for a non-CPAB–formatted control Alphabody could be detected in the cytosol of U87 glioblastoma cells, and demonstrates that CPAB-mediated cell

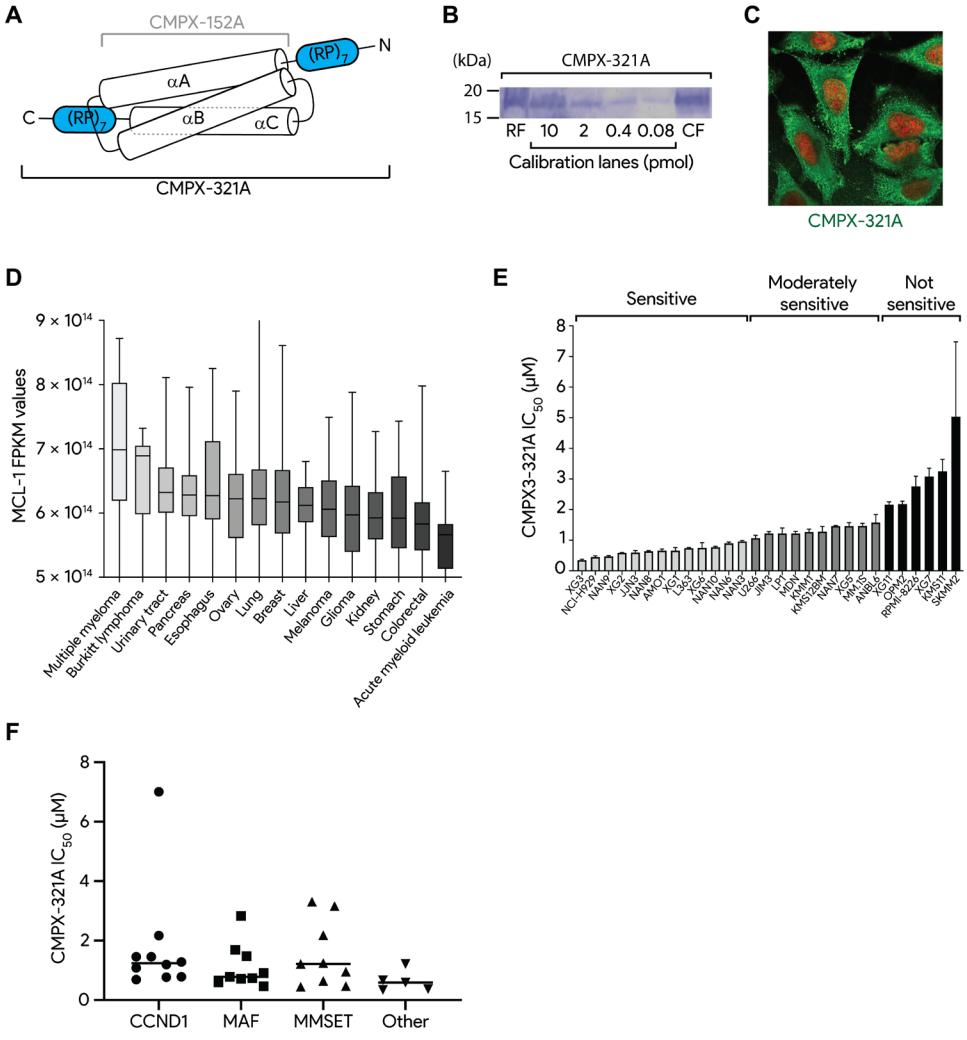

Fig. 2. CPAB-formatted CMPX-321A Alphabody efficiently enters MM cell lines to elicit MCL-1 inhibition. (**A**) Addition of an N- and C-terminal arginine-proline ($[RP]_7$) tag allows bilayer phospholipid crossing of CMPX-321A, the CPAB-formatted successor of CMPX-152A. (**B**) Western blot of the rest fraction (RF) and cytosolic fraction (CF) of NCI-H929 cells after 2 hours of incubation with 2 μM of the CPAB CMPX-321A. (**C**) Overlay of immunofluorescence experiments confirming the cell-penetrating capacity of CMPX-321A (green) in HeLa cells, after 30 min of incubation with 1 μM Alphabody. Nuclei are stained with Ruby stain (red). (**D**) RNA expression data (*41*, *42*) show that MCL-1 is substantially more expressed in MM cells compared to other cancer cell types, indicating that this cancer cell type might be MCL-1 dependent. (**E**) The cell killing potential of CMPX-321A was evaluated via a panel of 33 MM cell lines. Thirteen MM cell lines were shown to be very sensitive toward MCL-1 inhibition (IC_{50} < 1 μM), 10 cell lines were moderately sensitive (IC_{50} = 1 to 2 μM), and 6 cell lines were not sensitive to unresponsive (IC_{50} > 2 μM). (**F**) The cell killing potency of CMPX-321A cannot be predicted on the basis of the classical molecular signature of MM cell lines (CCDN1, MAF, MMSET, and others). FPKM, fragments per kilobase million.

penetration is independent of the presence of an intracellular protein target (fig. S3). Together, our data demonstrate that CPAB formatting of CMPX-152A resulted in an MCL-1–binding Alphabody that efficiently crosses the mammalian cell membrane, without affecting the stability of the Alphabody scaffold or its ability to bind to MCL-1 (tables S2 and S3). To our knowledge, this is the first known example of a cell-penetrating protein scaffold able to efficiently reach the intracellular space for binding to a therapeutically relevant protein target.

To evaluate the therapeutic potential of CPABs, we initially screened a panel of MCL-1–dependent cell lines with the CPAB-formatted CMPX-321A Alphabody targeting MCL-1. We found that several multiple myeloma (MM) cell lines displayed a high sensitivity to CMPX-321A treatment [IC_{50} (median inhibitory concentration) of <2 μM], while other cell lines—including colorectal, non–small cell lung, hepatocellular, ovarian, and acute myeloid cancer cell lines—were only moderately sensitive or not sensitive at all to MCL-1 inhibition using this anti–MCL-1 CPAB. The high sensitivity of MM cells to MCL-1 inhibition mediated by CMPX-321A appeared to positively correlate with MCL-1 expression levels. A survey of RNA expression data from the Broad Institute Cancer Cell Line Encyclopedia (Entrez ID 4170, accessed 29 March 2020) (*41*, *42*) shows that the expression levels of MCL-1 in MM cells is significantly higher than in other cancer types (Fig. 2D).

These findings prompted us to investigate the cell killing potential of the MCL-1 neutralizing Alphabody against a panel of 33 MM cell lines (Fig. 2E). Thirteen MM cell lines from this panel were highly sensitive to CMPX-321A, with IC_{50} values in the submicromolar range and with NCI-H929 being the most sensitive (IC_{50} value of 0.34 μM). In addition, 10 MM cell lines showed moderate sensitivity

(IC_{50} values of 1 to 2 μM), while 6 MM cell lines showed a weaker (IC_{50} values of 2 to 3.31 μM) or no response (IC_{50} value of 5.03 μM) to CMPX-321A treatment. Four cell lines were excluded from the experiment because they showed a high cell killing percentage (>40%) when treated with the non–MCL-1–binding CPAB-formatted prototypical Alphabody CMPX-322M, which is not expected to bind specifically to a known protein partner. MM can be divided in different genetic subsets based on their molecular profile, and the killing potential of CMPX-321A did not appear to be restricted to a specific genetic subset, indicating that all MM subgroups could benefit from MCL-1 inhibition (Fig. 2F). Together, our data suggest that the observed cell death of MM cell lines, induced by CMPX-321A in a concentration-dependent manner, is a consequence of MCL-1–driven inhibition.

Treatment with CPAB CMPX-321A induces BAK activation followed by apoptosis

Next, we sought to confirm that the cell killing effect in MM cell lines was mediated by cellular apoptosis. Using flow cytometry, we show that the observed cell death in NCI-H929 cells induced by CMPX-321A occurs via a dose-dependent activation of BAK, which is generally considered a hallmark event in apoptosis (Fig. 3B). To further confirm that the CMPX-321A–induced cell death was a consequence of BAK-mediated apoptosis, we performed additional propidium iodide (PI)/annexin V flow cytometry experiments in SU-DHL-4 cells. These cells were treated in triplicate for 6 hours with vehicle, CMPX-322M (2.5 to 5 μM), or CMPX-321A (2.5 to 5 μM) (Fig. 3C). The results show that the non–MCL-1 CPAB CMPX-322M induces apoptosis in only a minor fraction of the cells, while the MCL-1–targeting CPAB CMPX-321A induces a high percentage of apoptosis compared to the vehicle only ($P = 0.0032$). Upon CMPX-321A treatment (5 μM), a statistically higher percentage of apoptotic cells is observed compared to the cells that were treated with 2.5 and 5 μM of the control CMPX-322M ($P = 0.0167$ and $P = 0.02$, respectively) (Fig. 3, D and E). This clearly demonstrates that CMPX-321A induces BAK-driven cell death. To our knowledge, Alphabody CMPX-321A is the first non-Ig protein scaffold capable of translocating across a mammalian cell membrane to neutralize an intracellular target and to elicit a therapeutically relevant outcome.

Albumin binding increases serum half-life of CMPX-321A without compromising cell penetration

Because of their typical molecular weight of about 18 kDa, in vivo administered CPAB Alphabodies would be expected to undergo fast renal clearing, suggesting a need to increase their serum half-life to a therapeutically suitable window. Being aware that an increase in molecular weight could impede efficient cell penetration, we leveraged the crystal structure of *Finegoldia magna* protein G to engineer a minimal albumin-binding site (Fig. 4A) (*43*). *F. magna* protein G features a three-helix bundle fold, in which only the two shorter C-terminal α helices are involved in albumin binding. Substitution of the larger α helix of protein G by the C helix of CMPX-321A allowed engineering of an albumin-binding site with only a modest increase in molecular weight by 3.6 kDa. Last, we engineered a disulfide bond to tether the two albumin-binding helices to the Alphabody's C helix to enhance stability. The resulting Alphabody CMPX-383B combines the functionality of CMPX-321A with albumin-mediated half-life extension (HLE) technology, while retaining thermal stability and target affinity (tables S2 and S3). Biolayer interferometry (BLI) experiments further revealed that an exceptionally low dissociation velocity constant (k_d) is at the root of this ultrahigh affinity consistent with the expected hydrophobic nature of the interaction (Fig. 4B).

We reasoned that the affinity of the Alphabody for albumin should be carefully tuned to allow for albumin release before translocation into the cell. Initial immunofluorescence experiments in the presence of mouse serum albumin (MSA) revealed that a too high affinity for MSA impeded timely crossing of the lipid bilayer (Fig. 4D, right column). However, by substituting Gly^{40} in CMPX-383B for Ala, we were able to achieve a 40-fold reduction in the affinity of the Alphabody for serum albumin ($K_D = 7.5$ nM versus $K_D = 310$ nM; table S2). Whereas cellular uptake of CMPX-383B in the presence of MSA was slower compared to CMPX-321A (Fig. 4D, left column), this effect gradually diminished over time until the 16-hour time point, where no differences in cellular uptake could be observed (Fig. 4B, third row). Thus, it appears that albumin binding slows down, but does not prevent, the cellular uptake of the Alphabodies.

The effectiveness of HLE technology to extend the serum half-life of Alphabodies was confirmed by performing a pharmacokinetic study of administered Alphabody serum concentrations in healthy mice. CD-1 and CB-17 severe combined immunodeficient (SCID) mice were treated with a single intravenously administered bolus injection at 20 mg/kg of CMPX-321A and the half-life extended CMPX-383B, respectively. For both studies, Alphabody concentrations in serum and tissue samples were quantified using an in-house–developed solution enzyme-linked immunosorbent assay (ELISA) assay, which quantifies the concentration of intact and functionally active Alphabody in the samples. Measurement of serum levels demonstrated that the addition of HLE technology to the Alphabody substantially delays serum clearance (Fig. 4C). The calculated half-life ($t_{1/2}$) of CMPX-383B was 76 min, which was 10-fold higher than the $t_{1/2}$ of CMPX-321A ($t_{1/2}$ of 7.6 min).

CMPX-383B reduces tumor burden in MM xenograft models in vivo

To further probe the efficacy of Alphabodies with HLE optimization in vivo, we tested the effect of CMPX-383B in xenograft mice tumor models using MM cells. In a first series of xenograft experiments, two highly sensitive human MM cell lines NCI-H929 and MOLP-8 (in vitro IC_{50} for CMPX-383B of 0.45 and 0.82 μM, respectively) were subcutaneously injected in nonobese diabetic/SCID γ (NSG) mice ($n = 20$) (Fig. 5, A to C). Once the tumors reached an average volume of 80 mm^3 (range between 50 and 100 mm^3), treatment with CMPX-383B ($n = 10$) or vehicle control ($n = 10$) was initiated. CMPX-383B was administered once daily by intravenous injection at 20 mg/kg for 14 days (Fig. 5A). Daily administration of CMPX-383B (20 mg/kg) appeared to be well tolerated by the mice, and no toxic side effects by Alphabody CMPX-383B could be observed. During treatment, a significant delay in tumor growth was observed in the CPMX-383B–treated group compared to vehicle-treated mice in both NCI-H929 and MOLP-8 xenograft models ($P = 0.002$ and $P = 0.007$, respectively) (Fig. 5, B and C). Further monitoring after stopping the treatment in MOLP-8 xenografts revealed a near-significant prolonged delay in tumor growth during the week after the last treatment ($P = 0.051$) (fig. S1). In conclusion, our data show that CMPX-383B has a significant in vivo antitumor effect in two MM xenograft models.

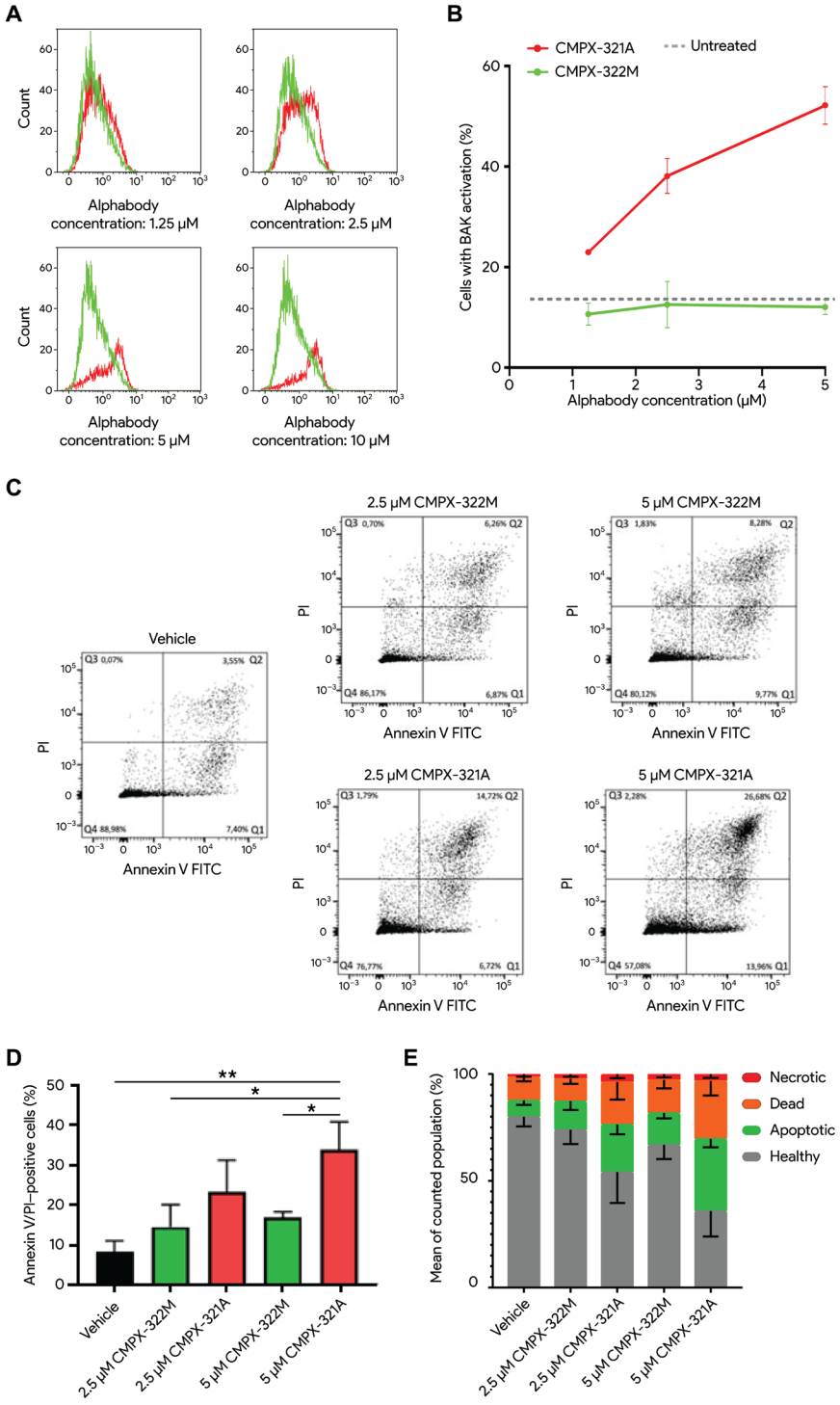

Fig. 3. CPAB CMPX-321A induces BAK-mediated apoptosis. (**A**) Flow cytometric histograms showing overlay plots of NCI-H929 cells treated with control CPAB CMPX-322M (green) and anti–MCL-1 CPAB CMPX-321A (red) that have been stained with an antibody specifically recognizing activated BAK ($n = 2$). (**B**) Percentage of BAK-activated–positive NCI-H929 cells following CPAB treatment with anti–MCL-1 CPAB CMPX-321A (red) and control CPAB CMPX-322M (green). CMPX-321A induces a dose-dependent BAK activation. The control CPAB is not inducing BAK activation and is comparable to nontreated cells ($n = 2$; error bars represent the SEM). (**C**) Two-dimensional dot plots showing SUD-HL-4 cells after 6 hours of treatment with vehicle, CMPX-322M (2.5 to 5 μM), or CMPX-321A (2.5 to 5 μM) after annexin V fluorescein isothiocyanate (FITC)/PI staining. These plots show four regions corresponding to early apoptotic cells ($PI^-/FITC^+$; Q1), late apoptotic cells ($PI^+/FITC^+$; Q2), necrotic cells ($PI^+/FITC^-$; Q3), and viable cells ($PI^-/FITC^-$; Q4). A higher percentage of apoptotic cells are observed after CMPX-321A treatment compared to the vehicle or CMPX-322M control. (**D**) Upon CMPX-321A treatment (5 μM), a statistically higher percentage of apoptotic cells is observed compared to the cells that were treated with 2.5 and 5 μM of the control CMPX-322M [$P = 0.0167$ and $P = 0.02$, respectively; one-way analysis of variance (ANOVA)] *: $P \leq 0.05$. **, $P \leq 0.01$. (**E**) Bar charts showing the mean percentage of necrotic, dead, apoptotic, and healthy SU-DHL-4 cells after 6 hours of vehicle, CMPX-322M, and CMPX-321A treatment ($n = 3$; error bars represent the SEM).

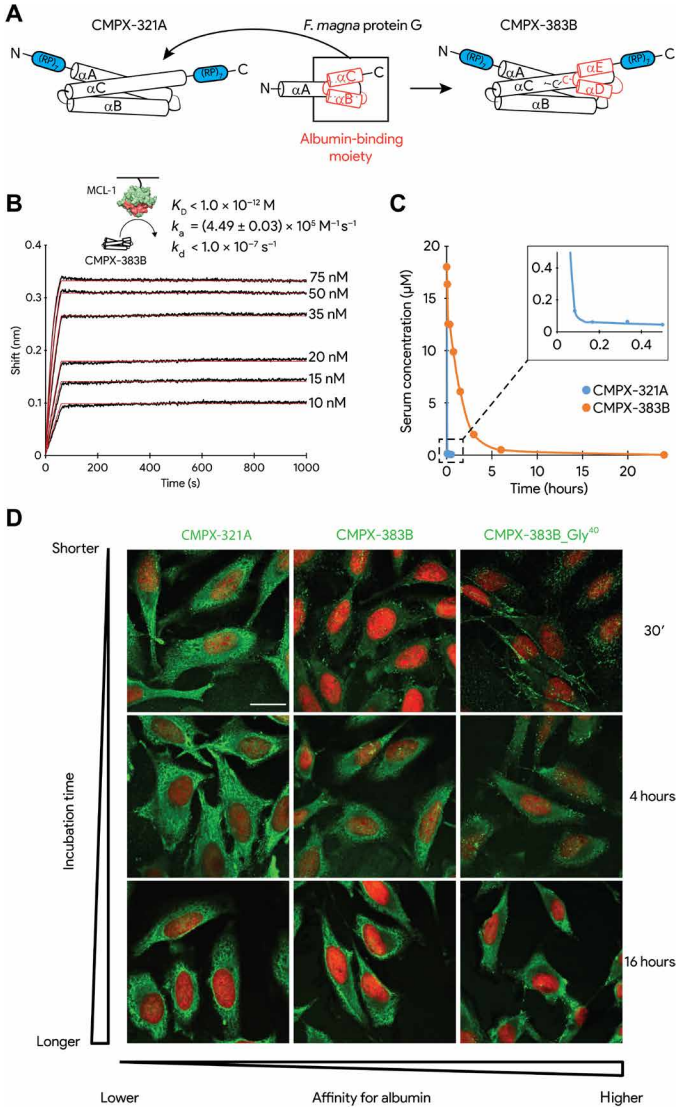

Fig. 4. Engineering of an albumin-binding site in CMPX-321A to increase its serum half-life. (**A**) By grafting only the short albumin-binding helices of *F. magna* protein G (red) on α-helix C of CMPX-321A, the resulting CPAB CMPX-383B is capable of binding albumin at the expense of only a 3.6-kDa increase in molecular weight. (**B**) Fitting of a 1:1 Langmuir binding model (red) to the BLI data traces (black) of the interaction CMPX-383B to immobilized glutathione *S*-transferase (GST)–$_{\Delta N\Delta C}$MCL-1, plotted as the spectral shift in function of time. Experiment was performed in duplicate. (**C**) Alphabody concentrations of CMPX-321A (blue) and the serum half-life extended Alphabody CMPX-383B (orange) in the sera of, respectively, three mice and two mice treated with a single intravenously administered bolus injection of 20 mg/kg. (**D**) Confocal microscopy experiments on HeLa cells in the presence of 10 μM MSA show that substitution of Gly^{40} by alanine (right and middle columns, respectively) allows a faster cellular uptake. After the indicated incubation time, cells were washed and probed for the presence of the Alphabody (green). The resulting immunofluorescence image was overlaid with a Ruby stain for the nuclei (red). Scale bar, 20 μm.

Structural basis of MCL-1 inhibition by CMPX-383B and of Alphabody HLE in serum

We pursued structural studies of CMPX-383B in complex with either MCL-1 or human serum albumin (HSA) by x-ray crystallography to elucidate the structural basis of the various design principles that were applied toward developing a CPAB with specificity for intracellular MCL-1 and favorable serum half-life. For our structural studies using MCL-1, we expressed and purified recombinant $_{\Delta N\Delta C}$MCL-1 (residues 172 to 320), a minimal construct that contains the BH3-binding groove and which results in higher protein expression and stability (*14*). A critical step in the biochemical isolation of the $_{\Delta N\Delta C}$MCL-1:CMPX-383B complex concerned the mixing of bacterial cell lysates after expression of the two proteins independently. The structural undertakings involving HSA used a second variant of CMPX-383B featuring an alternative implementation of the polar core layer. Purified and monodisperse protein samples for $_{\Delta N\Delta C}$MCL-1:CMPX-383B and HSA:CMPX-383B complexes led to optimized crystals that diffracted synchrotron x-rays to 2.26 and 3.3 Å, respectively (Table 1 and Fig. 6).

The crystal structure of the $_{\Delta N\Delta C}$MCL-1:CMPX-383B complex revealed the structural basis of MCL-1 inhibition and how CMPX-383B structurally accommodates for the negative design elements featuring a polar core layer (Fig. 6). To engage MCL-1, CMPX-383B deploys only the B helix to bind at the BH3-binding groove of MCL-1 (Fig. 6), which is presented by helices α2, α3, and α4 of MCL-1. The six MCL-1 residues that were grafted onto the B helix of CMPX-383B form the epicenter of the interaction, of which four make direct contacts with the hydrophobic platform of MCL-1 (Fig. 6A), while Asp^{B3d} and Arg^{B2g} of the Alphabody electrostatically interact with Arg^{263} and Asn^{260}, respectively, and the backbone of His^{152} and Val^{153} of $_{\Delta N\Delta C}$MCL-1 (Fig. 6B). The binding of the CMPX-383B B helix is further secured by interactions at both termini mediated by Glu^{49}, Lys^{52}, and Tyr^{70}, which seal the MCL-1 groove otherwise used to sequester antiapoptotic mediators. The B helix of CMPX-383B superimposes very well with the structure of the inhibitory MCL-1 helix $SAHB_D$ in complex with MCL-1 [root mean square deviation (RMSD) of 0.713 Å for 17 aligned Cα atoms] (Fig. 6G), including the hallmark arching imposed onto the inhibiting helix by MCL-1 (Fig. 6, E and F). The MCL-1–binding B helix of CMPX-383B displays a curvature of almost 30° toward its C terminus that coincides with a slight widening of the Alphabody core initiated at the polar core layer. The engineered polar core layer serves a twofold purpose to facilitate interaction of the core Asp^{B3d} of CMPX-383B with Arg^{263} of $_{\Delta N\Delta C}$MCL-1 and to mediate compliance with the conformational criteria imposed by the binding target. Collectively, this direct structural evidence illustrates how the Alphabody scaffold can be tailored to the particular structural landscape of the molecular target to bind with high specificity.

The crystal structure of the HSA:CMPX-383B complex allowed assessment of the possible structure-function consequences of HLE technology for the Alphabody scaffold (Fig. 6). Similar to the grafted MCL-1 inhibitory signature on the B helix, we observed that the appended D and E helices of CMPX-383B are virtually superimposable with the *F. magna* protein G template (RMSD of 0.49 Å over 48 Cα atoms) (Fig. 6H), providing direct evidence that the HLE technology allows an Alphabody to bind domain II of the albumin molecule using an extensive network of electrostatic interactions (Fig. 6, C and D). These interactions are reinforced by the burial of Phe^{118} and, to a lesser extent, Leu^{122} of the Alphabody into a hydrophobic pocket of HSA. Together, these two crystallographic structures highlight the engineerability and modularity of the Alphabody scaffold to accommodate tailored binding requirements to enhance pharmacokinetic performance.

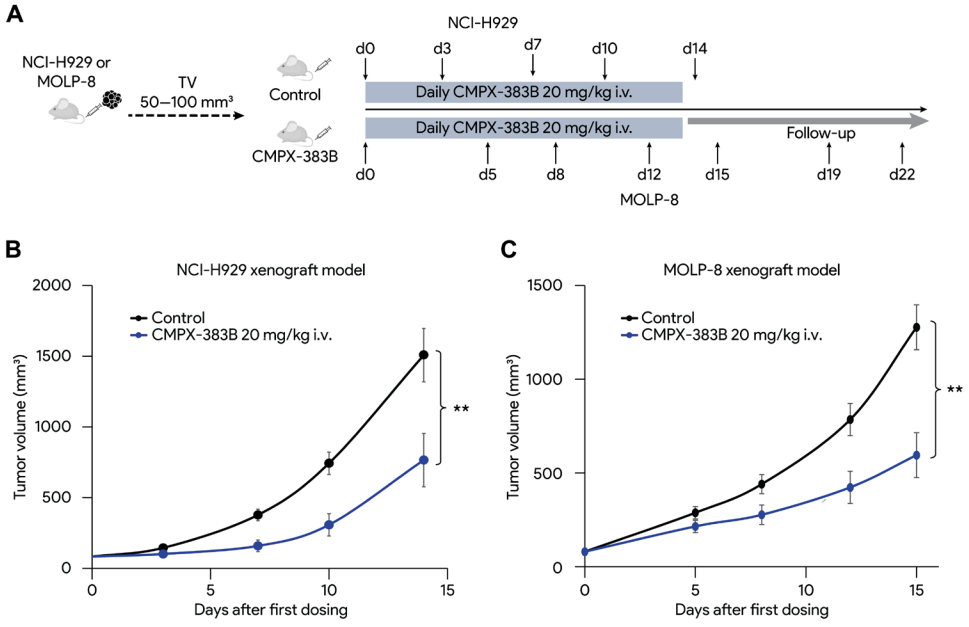

Fig. 5. In vivo antitumor effect of CMPX-383B in a MM xenograft model. (**A**) Therapy schedule followed for the treatment of both MM xenograft models. i.v., intravenously. (**B**) Treatment of NCI-H929 xenograft mice for 14 days with CMPX-383B ($n = 10$) significantly decreases tumor volume (TV) growth in CMPX-383B–treated mice, compared to vehicle ($n = 10$, $P = 0.002$). (**C**) Treatment of the MOLP-8 xenograft model with CMPX-383B ($n = 10$) results in a significant decrease in tumor volume growth during the treatment period compared to vehicle ($n = 10$, $P = 0.007$), $^{**}P \leq 0.01$.

DISCUSSION

It is estimated that only 10 to 14% of the druggable genome can be targeted by rule-of-five-compliant small molecules (*44*). As a result, protein-based scaffolds have emerged, featuring a higher specificity, lower off-target effects, and immunomodulating properties. However, both antibody- and nonantibody-based drugs lack the ability to cross the mammalian phospholipid bilayer, which limits their potential therapeutic space to targets that provide an extracellular or endosomal-mediated entry point. Our findings presented here show that the Alphabody protein scaffold can be designed, engineered, and formatted to display favorable serum half-life properties and to efficiently translocate across the mammalian cellular membrane to antagonize a tumorigenic protein:protein interface.

By aiming to develop Alphabodies targeting the well-known intracellular drug target MCL-1, an antiapoptotic protein up-regulated in multiple tumor types and correlated with therapy resistance (*15*–*21*, *45*), our study goes beyond the currently charted protein-based drug-targeting landscape. Although therapeutic inhibition of MCL-1 has been pursued for more than a decade, MCL-1 has proven to be recalcitrant to targeting by small molecules (*30*, *46*). Our design strategy showcases the engrafting of key binding determinants inspired from the interaction of MCL-1 with its inhibitory BH3 helix and other peptides onto the variable positions presented by the three-helix coiled-coil fold of the Alphabody scaffold. The resulting Alphabody CMPX-152A showed ultrahigh affinity in the low picomolar range for MCL-1. This tight binding has been postulated as a requirement for on-target affinity in MCL-1–dependent cell lines and is >20-fold tighter than the reported affinity of S63845, the most promising MCL-1 inhibitor to date (K_D of S63845, 190 pM) (*30*, *47*). The Alphabody achieves this high affinity via synergy of two key structural principles: (i) by harnessing fully the hydrophobic and electrostatic interaction opportunities presented at the epicenter of the BH3-binding groove of MCL-1 and by exploiting additional interactions at the ends of the α helix B to seal the BH3-binding groove and (ii) by exhibiting plasticity in its B helix to respond to the conformational requirements of the target interface. The latter feature differentiates this MCL-1–binding Alphabody from previous generations of the Alphabody scaffold and suggests that this property could be additionally exploited against new targets.

Engraftment of the MCL-1–binding residues onto the Alphabody scaffold required implementation of protein negative design manifested via the insertion of an aspartate residue into the hydrophobic inner core of the Alphabody and the concomitant engineering of an additional threonine in the aspartate-containing core layer, aimed to increase the energetic penalty of every other Alphabody conformation above the desired one. Although these negative design principles have been proposed to occur naturally during protein evolution, for instance, to prevent aggregation and to increase binding specificity, their application in de novo protein design has been limited (*32*, *48*–*50*).

Arguably, the most far-reaching outcome from our studies has been the implementation of a cellular uptake sequence motif that can enable efficient translocation of a candidate Alphabody across the cell membrane to reach an intracellular target, without loss of binding specificity. This addresses the most critical challenge in the use of protein scaffolds to reach intracellular drug targets. Initial exploration of cell-penetrating peptides, including the TAT sequence, at either the N or C terminus did not result in satisfactory levels of cell penetration. Furthermore, as an arginine residue frequently serves as a hotspot for protease recognition, we refrained from using a poly-arginine sequence as a tag for cellular uptake. Proline residues are hydrophobic by nature and considered to be less susceptible to proteolytic activity, and as initial modeling seemed to indicate that the conformational constraints on the peptide backbone could provide a

Table 1. Crystallographic data and refinement statistics. Values in parentheses correspond to the highest-resolution shell. RMS, root mean square.

Protein complex	CMPX-383B:$_{\Delta N \Delta C}$MCL-1 (PDB 6ZIE)	CMPX-383B:HSA (PDB 6ZL1)
Crystallization		
Crystallization condition	2% (w/v) PEG 3000	18% (w/v) PEG 3350
	0.1 M sodium acetate (pH 5.5)	0.1 M bis-tris (pH 6.8)
	0.2 M zinc acetate dihydrate	0.2 M ammonium phosphate
Cryoprotectant	30% (v/v) PEG 400	25% (w/v) PEG 3350, 10% (v/v) glycerol
Data collection		
Beamline*	ESRF ID23-2	PetraIII-P14
Wavelength (Å)*	0.872899	0.9763
Detector*	PILATUS 2M	PILATUS 6M-F
Space group*	P 6_1 2 2	C 2 2 2_1
a, b, c (Å); α, β, γ (°)*	69.70, 69.70, 261.29; 90, 90, 120	60.69, 231.37, 240.19; 90, 90, 90
Resolution (Å)*	44.33–2.3 (2.38–2.3)*	65.83–3.272 (3.39–3.27)†
Total reflections	156,815 (14,751)*	122,695 (5432)†
Unique reflections	17,663 (1682)*	25,902 (1168)†
Multiplicity	8.9 (8.8)*	4.7 (2.7)†
Spherical completeness (%)	99.68 (97.31)*	91.8 (45.1)†
Ellipsoidal completeness (%)	*n.a.*	91.57 (42.48)†
Mean *I*/σ	14.61 (0.84)*	8.47 (0.52)†
Wilson B-factor (Å^2)	55.48‡	84.53†
R-meas (%)	0.118 (2.519)*	0.118 (2.285)†
CC1/2 (%)	100 (38.8)*	99.7 (18.2)†
Refinement‡		
Resolution range (Å)	44.33–2.30	65.83–3.27
Reflections: refinement, cross-validation	17,659 (1677), 1059 (100)	24,554 (1125), 1271 (46)
R-work, R-free	0.2236§, 0.2628§	0.2445‖, 0.2786‖
Nonhydrogen atoms	2208	8926
Macromolecules, protein residues	2163, 273	8926, 1352
Ligand atoms, solvent atoms	14, 31	0, 0
RMS_{bonds} (Å), RMS_{angles} (°)	0.012, 1.17	0.013, 1.6
Ramachandran favored, allowed, outliers (%)	97.72, 2.28, 0	91.98, 6.73, 1.29
Rotamer outliers (%)	4.78	9.38
Clashscore	2.96	7.49
Average B-factor (Å^2)	39.88	97.99
Macromolecules	39.18	97.99
Ligands	83.37	0
Solvent atoms	69.03	0
TLS groups	2	5

*Values reported by the XDS Program Package. †Values reported by STARANISO anisotropy & Bayesian estimation server. ‡Values reported by Phenix. §Values reported by PDB-REDO. ‖Final refinement was performed in BUSTER 2.10.3. TLS, Translation-Libration-Screw-rotation; n.a., not applicable.

good clustering of the arginine guanidium groups, we gradually converged onto the $[RP]_7$ tag. Last, although cellular uptake was also possible using a single N- or C-terminal CPAB tag, the highest efficiency of cell penetration was observed when CPAB sequences were present at both termini. We showed that such an anti–MCL-1 Alphabody, when decorated with CPAB tags, was a potent inhibitor of several MCL-1–dependent oncogenic cell lines and induced apoptosis in a dose-dependent manner by activating the BAK-dependent mitochondrial apoptotic

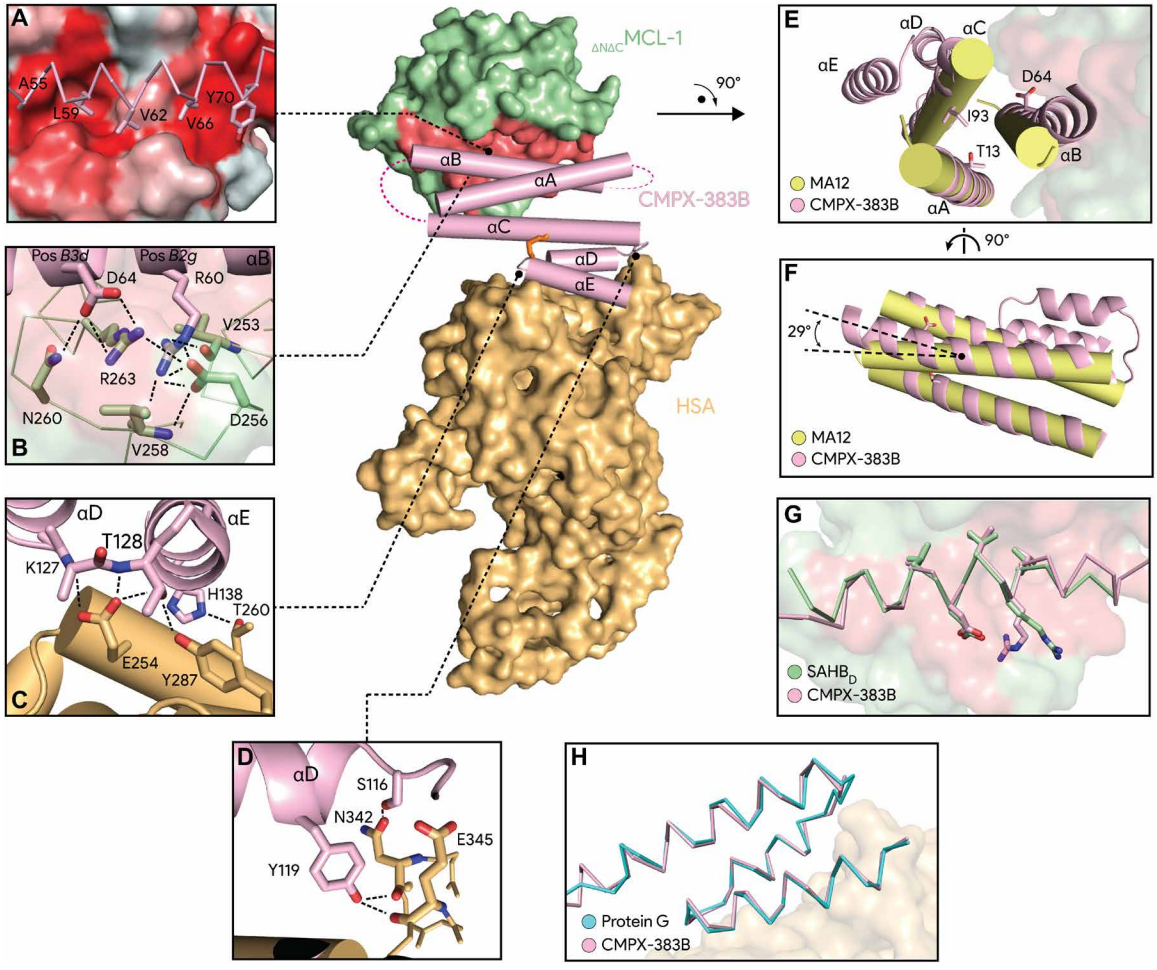

Fig. 6. Structural validation of the applied engineering strategies. Middle: Structural superposition of crystal structures featuring CMPX-383B (pink) in complex with either $_{\Delta N\Delta C}$MCL-1 (green) or HSA (orange). Alphabody CMPX-383B is shown in cartoon representation. The linker regions between α-helix A and B and between α helices B and C are represented as dashed lines. The cysteine disulfide bridge that covalently links α helices E to C (dark orange) is shown in stick representation. $_{\Delta N\Delta C}$MCL-1 and HSA are shown in surface representation. The BH3-binding groove of $_{\Delta N\Delta C}$MCL-1 is colored red. (**A**) Detailed view of the hydrophobic interface between α helices B of CMPX-383B and the BH3-binding groove of $_{\Delta N\Delta C}$MCL-1. α Helix B of CMPX-383B is shown as ribbon diagram, and $_{\Delta N\Delta C}$MCL-1 is shown in surface representation and colored according to the Eisenberg hydrophobicity scale (red is more hydrophobic). (**B**) Detailed view of the electrostatic interactions around Asp^{64} and Arg^{60} of CMPX-383B at the BH3-binding groove of $_{\Delta N\Delta C}$MCL-1. (**C** and **D**) Detailed views on how CMPX-383B engages HSA using predominantly electrostatic interactions at α helix D, the αD-αE loop, and α helix E. (**E** and **F**) Structural superposition of CMPX-383B (pink, canonical helix representation) and the canonical IL-23 binding Alphabody MA12 (yellow; cylindrical helix presentation, generated using PDB code 5MJ3), highlighting the distinct arching of α helix B of CMPX-383B allowing a full occupancy of the BH3-binding groove of $_{\Delta N\Delta C}$MCL-1 (surface representation). (**G**) Structural superposition of the inhibitory MCL-1 helix SAHB$_D$ (green; PDB code 3MK8) with α helix B of CMPX-383B (pink), both when in complex with MCL-1 (surface representation). (**H**) Structural superimposition of the albumin-binding moiety of *F. magna* protein G (cyan; generated using PDB code 1TF0) and α helices C, D, and E of CMPX-383B (pink), both bound to HSA (orange; surface representation).

pathway. Similar to other selective MCL-1 inhibitors (*51*), treatment with a cell-penetrating anti–MCL-1 Alphabody results in a rapid induction of cell death via apoptosis in hematological malignancies such as MM, leukemia, and lymphoma. Thus, we expect that such an approach cannot only be widely applied to Alphabodies developed against other intracellular targets but also to other protein scaffolds as well. To date, 20 different non-Ig–like scaffolds have been reported that are often directed against protein-protein interfaces and find applications in therapeutics, diagnostics, imaging, and research [reviewed in (*5*, *52*, *53*)]. Notably, Stefin A Quadruple Mutant-Tracy (SQT) scaffolds fused to BH3 sequences of Puma, Bim, Noxa, and Bad have been successfully deployed to provide insights into BH3-mediated induction of apoptosis (*54*). However, to our knowledge, none of these scaffold proteins has been further engineered to include both cell penetration and HLE technology by default. Furthermore, although surface cationization and incorporation of polycantionic sequences have been reported to endow small proteins such as single-domain antibodies, with cell-penetrating capabilities (*55*–*60*), their application has, however, been restricted to proof-of-concept experiments only, as many therapeutic proteins arguably do not readily tolerate surface cationization (*55*). However, the recent reporting of an α-helical mimic of nuclear factor kappa-B essential modulator (NEMO) capable of antagonizing the intracellular interaction of NEMO with a viral oncoprotein (*61*) illustrates that interrogation of intracellular targets by exogenously administered protein-based antagonists is decisively moving forward. Nevertheless, it is clear that the field is still at its infancy when it comes to protein scaffolds that can be tailored

to a variety of extracellular and intracellular binding epitopes via a combination of computational design and platform technologies comprising biopanning and binder selection.

A second advance from our studies concerns the engineering of serum HLE technology onto the Alphabody scaffold without interfering with cell penetration or target binding. The key challenge was to achieve extension of the serum half-life of CPAB-formatted Alphabodies, which is typically enhanced by increasing the mass of the protein, while maintaining a low molecular weight to preserve efficient cell penetration. We succeeded in resolving this dichotomy by grafting, rather than adding, the smallest albumin-binding helices of *F. magna* protein G onto the MCL-1–binding Alphabody CMPX-383B. In principle, this can be applied to increase the serum half-life of other scaffolds as well, although engrafting of the albumin-binding domain requires the availability of a helical surface, preferably at one of the termini of the polypeptide. A survey of protein scaffolds and the advent of deep learning approaches in protein design and engineering (*52*, *62*–*64*) suggest that the grafting of molecular properties within a helical protein scaffold, thereby avoiding the concatenation of additional protein modules, could find broad application.

We have demonstrated the benefit of combining these design implementations in Alphabody CMPX-383B by alleviating tumor burden in vivo via xenograft experiments based on MM cell lines. These findings establish the potential of the Alphabody scaffold in antagonizing therapeutically relevant intracellular protein interfaces in vivo. Our focus on MCL-1 as a proof of concept for our strategy was rooted at the α-helical nature of confirmed inhibitors and the challenging character of targeting this interface with small molecules. Recently, several potent and selective MCL-1 inhibitors have been reported, some of which have entered clinical trials (NCT03218683, NCT03672695, NCT02979366, NCT02675452, and NCT03797261) (*65*–*67*). As our study sought to explore the Alphabody's potential within a therapeutically relevant scenario rather than developing a novel anticancer drug candidate, we refrained from doing head-to-head comparisons with known MCL-1 inhibitors.

Last, we are left to wonder about the two orders of magnitude difference between the determined binding affinity and observed potency of CMPX-383B (K_D of 8 pM versus IC_{50} of 0.5 to 1 μM in NCI-H929 MM cells). Whereas the affinity of CMPX-383B was determined for free MCL-1, intracellular MCL-1 is always in complex with either BIM or BAK at the mitochondrion. If a candidate inhibitor should target this complex, then the binding of the inhibitor on MCL-1 will depend on the kinetics of BAK/BIM release from MCL-1 and on the dynamics by which newly transcribed MCL-1 becomes available for complex formation with BAK or BIM. The biological effect (i.e., cell killing) will be triggered upon reaching a certain level of target occupancy as determined by the biology of MCL-1. At the outset, the concentration of inhibitor may exceed the intrinsic K_D for the target at the IC_{50}. However, for CMPX-383B, the apparent discrepancy between K_D and IC_{50} appears to be more pronounced as compared to a small-molecule MCL-1 inhibitor such as S63845, evaluated against the same cell types (*47*). S63845 shows a K_D of approximately 0.19 nM for human MCL-1 and single-digit nanomolar potency against NCI-H929. Hence, there may be other factors, not related to the biology of MCL-1, that may explain why one compound shows a much higher IC_{50} as compared to another compound, while both exhibit strong target binding. This could be reconciled by differences in the intracellular accumulation of the respective inhibitory molecules, their intracellular mobility, or the accessibility of the target binding moieties as affected by cellular compartmentalization and cytosolic macromolecular crowding (*68*–*74*). In light of molecular size considerations, it would be tempting to suggest that these effects might be more pronounced for biologicals, such as CMPX-383B. However, AMG-176, a small-molecule inhibitor of MCL-1 (*67*), also shows a pronounced apparent discrepancy between IC_{50} and K_D (IC_{50} of 0.24 μM in OPM2 cell viability versus a picomolar binding affinity). Hence, it is clear that more comparative research will be needed to better understand the role of these parameters in the targeting of intracellular proteins and to consolidate binding behaviors given a particular molecular and cellular context. Collectively, the work we have presented here provides protein design principles, technologies, and proof of concept to enable the integration of protein scaffolds in strategies to antagonize intracellular therapeutic targets.

MATERIALS AND METHODS

Expression and purification of Alphabodies

Alphabodies were recombinantly produced as reported previously (*7*). Briefly, recombinant production of Alphabodies with an N-terminal decahistidine tag was performed in BL21(DE3)pLysS cells (Life Technologies), grown in Luria-Bertani medium at 37°C. At an optical density at 600 nm (OD_{600nm}) of 0.6, expression was induced by an addition of 1 mM isopropyl-β-D-thiogalactopyranoside. Expression was allowed for 4 hours at 37°C, after which cells were harvested by centrifugation, resuspended in tris buffer, and frozen at −80°C. Cell lysis was performed by thawing and sonication in the presence of deoxyribonuclease I (DNase I) and $MgCl_2$, after which the suspension was cleared by centrifugation at 40,000*g*. Alphabodies were isolated from the soluble fraction using a 5-ml immobilized metal affinity chromatography (IMAC) HP Ni Sepharose column (GE Healthcare), followed by a polishing and desalting step, performed on a Superdex 75 size exclusion column (GE Healthcare) equilibrated in phosphate-buffered saline (PBS).

Production and purification of recombinant human MCL-1

The reference sequences of the complementary DNA (cDNA) encoding for MCL-1 residues Asp^{172}-Gly^{327} ($_{\Delta N \Delta C}$MCL-1) (NM_001197320.1) were synthesized by GeneArt as a cotranslational fusion with glutathione *S*-transferase (GST) and cloned in the pET42 vector (Novagen). The GST–MCL-1 fusion protein was expressed in BL21(DE3)pLysS cells (Life Technologies). Cultures were grown at 37°C in LB supplemented with kanamycin (100 μg/ml). At an OD_{600nm} of 0.6, expression was induced by addition of 1 mM isopropylthio-β-galactoside. Expression was allowed for 4 hours at 30°C, after which cells were harvested by centrifugation, resuspended in PBS buffer, and frozen at −80°C. Cell lysis was performed by thawing and sonication in the presence of DNase I, $MgCl_2$, and AEBSF Protease Inhibitor (Thermo Fisher Scientific), after which the suspension was cleared by centrifugation at 40,000*g*. Purification of the fusion construct was performed from the soluble fraction using GST Trap FF column (GE Healthcare), followed by a polishing step performed on a Superdex 75 size exclusion column (GE Healthcare) equilibrated in tris buffer.

Solution ELISA assays for MCL-1 affinity determination

A Nunc plate was coated with anti-M13 (1 μg/ml; Thermo Fisher Scientific) in PBS for 2 hours at room temperature (RT). The plate

was then blocked with 2% skimmed milk in PBS for 2 hours at RT while shaking. A proprietary Alphabody-displaying phage with high affinity for MCL-1 was added in PBS + 1% bovine serum albumin (BSA) for 1 hour at RT while shaking. In parallel with previous steps, a mixture of 50 pM GST-tagged MCL-1 and a dilution series of test Alphabody (seven twofold dilutions starting at 2 nM plus a blank) in PBS + 1% BSA was preincubated in a deep-well plate for 4 hours at RT. In addition, a "calibrator" dilution series of GST-tagged MCL-1 (seven twofold dilutions starting at 100 pM plus a blank) in PBS + 1% BSA was prepared. The MCL-1–Alphabody mixtures and the calibrator series were then transferred to the ELISA plate in duplicate (two columns for each series) and incubated for another 1 hour at RT while shaking. Detection of bound GST–MCL-1 was performed with 1:5000 goat anti–GST–horseradish peroxidase (HRP) (Abcam) in PBS + 1% BSA for 30 min at RT while shaking. After each incubation step, the plate was washed 4× with PBS containing 0.05% Tween 20, except after the incubation step of the mixture and calibrator samples where the plate was washed 12 times. The plate was developed with SureBlue, and the reaction was stopped with H_2SO_4. ODs were read at 450 nm. For the calculation of Alphabody–MCL-1 affinity, the OD signals from the calibrator series were first fitted to a sigmoid function, the latter providing the relationship between the measured ODs and free GST–MCL-1. Using this relationship, the OD values measured for the Alphabody–MCL-1 mixtures were converted to free GST–MCL-1 concentrations, and the latter were then fitted to the quadratic equation for Alphabody–MCL-1 binding, using the solution K_D as parameter.

Solution ELISA assays for albumin affinity determination

An ELISA assay was elaborated for CPAB-albumin affinity determination exploiting the observation that CPABs show affinity for skimmed milk–blocked Nunc plates but not when bound to albumin. A Nunc plate was blocked O/N with PBS + 2% skimmed milk in PBS at 4°C. A mixture of 8 nM CPAB CMPX-383B and dilution series of human, rat or mouse serum albumin was prepared (seven threefold dilutions starting at 10 μM plus a blank) in 100 mM tris + 100 mM NaCl + 1% BSA (at pH 7.4) in deep-well plates and preincubated for 30 min at RT while shaking. In addition, a calibrator dilution series of CPAB (seven threefold dilutions starting at 100 nM plus a blank) in 100 mM tris + 100 mM NaCl + 1% BSA (at pH 7.4) was prepared. The albumin-CPAB mixtures and the calibrator series were then transferred to the ELISA plate in duplicate (two columns for each series) and incubated for another 30 min at RT while shaking. Detection of plate-bound CPAB was performed with 1/5000 anti-V5-HRP (Invitrogen, R961-25) in PBS + 0.1% BSA for 30 min at RT while shaking. After each incubation step, the plate was washed 4× with PBS containing 0.05% Tween 20. All further steps, including the conversion of OD values into free CPAB concentrations using the calibrator series and the fitting of solution K_D values, were the same as for MCL-1 affinity determination.

Circular dichroism experiments

Before the measurement, Alphabodies, stored in 20 mM Hepes (pH 7.2) and 150 mM NaCl, were centrifuged and diluted to 200 to 340 μg/ml in PBS with indicated concentrations of GuHCl. The fraction of α-helical content was calculated from the molar residue ellipticity (MRE) at 222 nm. For determination of the thermal stability, the up scan (5° to 95°C) was immediately followed by a down scan (95° to 5°C). The reported T_M value was calculated as the average temperature of the two minima. Reported values for reversibility of folding were calculated as the ratio of MRE at 25°C from the down scan versus the up scan.

Western blot analysis of Alphabody cellular uptake and determination of intracellular cytosolic Alphabody concentrations

NCI-H929 cells were seeded in 12-well plates (Greiner Bio-One, #665180) at a density of 6×10^5 cells per well in standard culture medium. After overnight growth, either Alphabody CMPX-321A or the non-CPAB–formatted Alphabody MB23 was added to a final concentration of 2 μM and incubated for either 2 or 6 hours at 37°C. After incubation, the cells were harvested, and their cell content was fractionated into a cytosolic and rest fraction (Abcam Cytosol/Particulate Rapid Separation Kit, #ab65398) and loaded on SDS–polyacrylamide gel electrophoresis (PAGE) (10% Criterion XT bis-tris gel, Bio-Rad) together with a dilution series of CMPX-321A. Protein content was electroblotted to a 0.2 μM polyvinylidene difluoride (PVDF) membrane (Trans-Blot Turbo Midi 0.2-μm PVDF, Bio-Rad). After blocking and washing, Alphabodies were detected using a mix of antibodies (anti-histidine tagged antibody clone HIS.H8, Merck, #05-949; 1/2000 diluted and supplemented with two proprietary monoclonal antibodies recognizing a common epitope in the α helix B) and visualized using an anti-mouse alkaline phosphatase (AP) secondary antibody (anti-mouse IgG AP conjugate, Promega, #S3728; 1/5000 diluted).

The calculation of cytosolic concentration is based on in-house confocal microscopy experiments. These allowed us to estimate the volume of NCI-H929 cell to be approximately 1 pl. The intensity of the CMPX-321A signal in the cytosolic fraction of Fig. 2B was higher than the 17 μM (10 pmol) calibrator lane. Given that the isolated cytosolic fraction of NCI-H929 cells is even lower than the total cell volume (in which other organelles, such as the relatively big nucleus, are present), we can infer that the intracellular concentration of CMPX-321A exceeds 17 μM as well.

Immunofluorescence experiments on HeLa cells

HeLa cells were seeded in eight-well Nunc Lab-Tek Chamber Slides (Thermo Fisher Scientific, #177402), treated with 1 μM MCL-1–targeting CPAB in the presence or absence of 10 μM MSA for the indicated time points. Cells were fixed and permeabilized with 100% methanol and blocked with 2% BSA in Dulbecco's PBS with 0.05% Triton X-100 blocking (1 hour at RT), before incubating with anti-V5 tag monoclonal (1 hour at RT; Thermo Fisher Scientific, #R960-25). Primary antibody was visualized using anti-mouse Alexa Fluor 488–conjugated antibody (45 min at RT; Thermo Fisher Scientific, #A-21202). Vybrant DyeCycle Ruby stain (30 min at RT; Thermo Fisher Scientific, #10115414) was used to dye the nuclei. Chambers were removed and coverslips mounted with fluorescence mounting medium (Dako, #S3023). Images were obtained using a Zeiss LSM 510 META confocal microscope and analyzed using Fiji ImageJ.

Western blot analysis to determine cytoplasmatic presence of CMPX-321A and CMPX-322M in SU-DHL-4 cells

SU-DHL-4 cells were treated in vitro with either vehicle or 1.25, 2.5, or 5 μM anti–MCL-1 CPAB (CMPX-321A) and a control CPAB (CMPX-322M) for 2 hours. After washing the cells with PBS, cell pellets were resuspended in lysis buffer [25 mM tris-HCl (pH 7.4),

150 mM NaCl, 0.1% NP-40, 2.5 mM $MgCl_2$, and 5% glycerol] and lysed for 15 min on ice. Lysates of total protein were separated by SDS-PAGE, electrotransferred to nitrocellulose membranes, and analyzed for the presence of the Alphabodies using a V5 antibody (Invitrogen, R960-25). Protein detection was performed with the Chemidoc MP Imager and the Image Lab software.

In vitro treatment of MM cell lines with CMPX-321A

Human myeloma cell lines were derived from primary myeloma cells cultured in RPMI 1640 medium supplemented with 5% fetal calf serum and recombinant IL-6 (3 ng/ml) for IL-6–dependent cell lines. Cell viability was measured using CellTiter-Glo luminescent cell viability assay from Promega. As control and to calculate percentages of cell viability, at least triplicates of cells in medium only (without test compound) were included on every plate. Luminescence signal of these wells (cells without test compound) corresponds to 100% cell viability. The start concentration of CMPX-321A and CMPX-322M was 5 μM with a twofold dilution step and seven concentration points (5 to 2.5 to 1.25 to 0.625 to 0.313 to 0.156 to 0.078 μM). As a buffer control, dilutions of buffer corresponding to the seven dilutions of test compounds were included. All experiments were repeated three times, and each experimental condition, including the buffer control, was repeated in duplicate wells in each experiment. The inhibition effect was calculated after 72 hours of incubation with the following formula: % viability = (luminescence of treated cells / luminescence of cells with medium only) × 100. IC_{50} values were calculated using the GraphPad Prism software and a four-parameter nonlinear regression with 100% cell survival in medium as top constraint and 0% cell survival as bottom constraint.

BAK activation assay

NCI-H929 cells were treated with twofold dilutions starting at 10 μM CPABs in 500 μl of complete cell culture medium containing 10% fetal bovine serum. Cells were incubated for 4 hours at 37°C. After CPAB treatment, cells were washed with PBS and permeabilized using the Cytofix/Cytoperm Fixation/Permeabilization Solution Kit (BD Biosciences) following the manufacturer's recommendations. Activated BAK was detected with the primary anti-BAK antibody TC-100 (Merck Millipore). After a washing step, detection of the primary anti-BAK antibody was performed with an Alexa Fluor 488–labeled secondary anti-mouse antibody. To exclude dead cells from data analysis, the LIVE/DEAD Fixable Near-IR Dead Cell Stain (Invitrogen) was included. Last, cells were washed once and measured on a BD LSRFortessa cell analyzer. The flow cytometry data were analyzed using either FACSDIVA or FlowJo software.

Annexin V/PI staining

Annexin V/PI double-staining kit (BD Biosciences, 556547) was used to detect cell apoptosis via flow cytofluorimetric analysis. SUD-HL-4 cells were treated in triplicate for 6 hours with either vehicle [20 mM Hepes (pH 7.2) and 150 mM NaCl], CMPX-322M (2.5 to 5 μM), or CMPX-321A (2.5 to 5 μM). After treatment, cells were washed with cold PBS, and the protocol of the annexin V/PI kit was followed as recommended by the manufacturer. During this experiment, unstained, single annexin V and PI stains were included for further flow analysis. The data generated by flow cytometry were analyzed using the FlowJo software (BD Biosciences) and are plotted in two-dimensional dot plots in which annexin V–fluorescein isothiocyanate (FITC) is represented versus PI. These plots show four regions corresponding to apoptotic cells ($PI^-/FITC^-$; Q1), late apoptotic cells ($PI^+/FITC^+$; Q2), viable cells ($PI^+/FITC^-$; Q3), and necrotic cells ($PI^-/FITC^-$; Q4). Statistical analysis was performed using the GraphPad Prism 8.3.0 software [one-way analysis of variance (ANOVA)].

BLI experiments

BLI experiments were performed at 25°C in kinetic buffer [PBS (pH 7.4), 0.02% (v/v) Tween 20, and 0.1% (w/v) BSA] using an Octet RED96 machine (Sartorius). Anti-GST biosensors (Sartorius, 18-5096) were functionalized with GST-$_{\Delta N \Delta C}$MCL-1, a response shift of 1 nm, and dipped into a solution containing indicated concentrations of the Alphabody. Nonfunctionalized biosensors were used during the assay to determine nonspecific binding of the Alphabodies. Sensor traces of zero concentration conditions were used for single reference subtraction. A 1:1 ligand model was fitted to all data using the FortéBio Data Analysis 9.0.0.4 software. For each experiment, a technical replicate was performed.

CMPX-383B test item handling for in vivo experiments

The vials containing the Alphabody CMPX-383B were stored at −80°C until the day of use. On the day of use, CMPX-383B was thawed for 30 min in a water bath at 37°C. Before use, the test substance was visually inspected for sign of turbidity. If turbidity was observed, then the vial of the test substance was put in the water bath at 37°C for another 15 min. The test substance was used within 1 hour of thawing for all in vivo experiments.

In vivo treatment of MM xenograft models

A MOLP-8 subcutaneous xenograft model was established in 20 NSG female mice at the age of 6 to 8 weeks by injecting 1×10^7 in human MM MOLP-8 cells at the right flank region. Before tumor cell inoculation, each animal was pretreated for 2 days with a daily intraperitoneal injection of cyclophosphamide (150 mg/kg) to facilitate engraftment of the MOLP-8 cells. Once the tumors reached an average volume of 80 mm^3 (range between 50 and 100 mm^3), mice were randomized into two groups and either treated daily with vehicle [20 mM Hepes (pH 7.2) and 150 mM NaCl] or CMPX-383B (20 mg/kg of body weight) for 14 consecutive days. Tumor volume was measured twice a week using a caliper until 20 days after the last treatment administration. Mice were closely monitored and euthanized if tumor volume reaches 3000 mm^3 or any humane end points.

For the NCI-H929 subcutaneous xenograft model, 20 female CB-17 SCID mice (nomenclature: CB-17/Icr-*PrKDcscid*/Rj) at the age of 8 weeks were subcutaneously inoculated with 5×10^6 NCI-H929 tumor cells into their right flank. Tumor volume was measured twice a week by caliper, and body weight was determined in parallel. Once an average tumor volume of 80 mm^3 was reached, animals were randomized into two groups. The animals received once daily, repeated intravenous doses of CMPX-383B (20 mg/kg) or vehicle [20 mM Hepes (pH 7.2) and 150 mM NaCl]. All experiments involving mice were performed by the biopharmaceutical company Heidelberg Pharma (Germany), and all ethical guidelines were followed as imposed by the European Union.

Statistical analysis of in vivo tumor evolution in xenograft models

Special consideration was given to the statistical analysis of the acquired data. Recognizing the presence of correlated observations (i.e., the response is measured repeatedly on a set of mice), we analyzed

tumor volumes as longitudinal data, also known as repeated measurements. The defining feature of longitudinal data is the possibility to characterize changes over time (e.g., tumor progression) and factors that influence that change. This is in contrast to the more commonly performed analysis at each time point, which only provides information about the differences in treatment effects at that specific time point and hence does not consider the evolution in treatment effects. Ordinary linear regression can model the evolution in outcome over time but does not accommodate for the correlation between observations. Therefore, in repeated-measurements analysis, the aim is not only to characterize changes over time and factors that influence that change but also to model the correlation across time within subjects, to get better estimates of treatment effects and the error.

We analyzed tumor volumes and hCD45 percentages as repeated measurements using the method of residual maximum likelihood, as implemented in Genstat version 20. Briefly, a linear mixed model (random terms underlined) of the form y = treatment + time + treatment × time + mouse × time was fitted to the longitudinal data. The term mouse × time represents the residual error term with dependent errors because the measurements are taken in the same individual, causing correlations among observations. Several covariance models were fitted to the data to account for the correlation present in the data. The autoregressive correlation model of order 1 (AR1) with times of measurement set at equal intervals was selected as the best fitted model based on the Akaike's information criterion coefficient (AIC) for analysis of tumor volumes. The AR covariance model assumes that correlation between observations decays as the measurements are collected further apart in time. The first order refers to the fact that only recent (t − 1) observations affect the current observations made at time point t. The antedependence correlation model of order 1 (ANTE1) with times of measurement set at unequal intervals was selected as the best fitted model based on the AIC for analysis of hCD45 percentages. The ANTE1 covariance model assumes that correlation between observations decays as the measurements are collected further apart in time, just like the AR covariance model does, but allows for changes in correlation structure over time. In addition, the ANTE covariance model allows for unequal variances across time. The significance of the fixed terms in the mixed model was assessed using an approximate F test as implemented in Genstat version 20.

Expression and purification of recombinant protein complexes for crystallization

The reference sequences of the cDNA encoding for MCL-1 residues Asp^{172}-Gly^{327} ($_{\Delta N\Delta C}$MCL-1) (NM_001197320.1) were synthesized by GeneArt and were a gift from Complix N.V. A GST fusion construct was created in which $_{\Delta N\Delta C}$MCL-1 was cotranslationally fused to GST, separated by a thrombin recognition sequence. The fusion construct was cloned in the pET15b vector (Novagen) using Nco I and Bam HI restriction sites. In parallel, a construct was created in which crystallography optimized variants of CMPX-383B lacking the CPAB sequences could be expressed in the pET15b vector with a thrombin-removable hexahistine sequence.

For isolation of the $_{\Delta N\Delta C}$MCL-1:Alphabody complex, *Escherichia coli* BL21(DE3) strains were transformed with the expression construct of either GST–$_{\Delta N\Delta C}$MCL-1 or the Alphabody. Single colonies of both plates were used to inoculate 10 ml of LB medium for overnight growth. Next day, both precultures were used to inoculate 3 liters of LB medium per construct. At OD_{600nm} of 0.6, expression was induced with 1 mM isopropyl-β-D-thiogalactopyranoside final concentration. GST–$_{\Delta N\Delta C}$MCL-1 was expressed for 4 hours at 28°C, after which the bacteria were harvested by centrifugation (6000*g* for 15 min at 4°C), and the cellular paste was stored at −80°C. Expression of the Alphabody was continued overnight. Next day, the bacteria expressing the Alphabody were harvested, while the bacterial pellet with GST–$_{\Delta N\Delta C}$MCL-1 was thawed. Both pellets were resuspended in 45 ml of phosphate buffer [300 mM sodium phosphate buffer (pH 7.0) and 300 mM NaCl] per liter of expression culture and mixed together before cell lysis. The cells were lysed by sonication on a Q500-220 QSonica sonicator (run time of 4 min with 30-s pulses at 80% output interspersed with 30 s of down time) and centrifuged for 30 min at 20,000*g*. The supernatant of both lysates was collected, filtrated through a 0.22-μm filter, and mixed. This mixture was then lastly applied overnight on two 1-ml GSTrap (GE Healthcare) at a flow speed of 0.1 ml/min. Next day, both columns were extensively washed with phosphate buffer, after which 6 U of biotinylated thrombin (Novagen) was injected. After injection, the columns were detached and incubated overnight at RT. Next day, elution of thrombin-cleaved $_{\Delta N\Delta C}$MCL-1, alone or in complex with thrombin-cleaved Alphabody, was performed by restoring the flow on the GSTrap columns. $_{\Delta N\Delta C}$MCL-1:CMPX-383B was lastly separated from thrombin and $_{\Delta N\Delta C}$MCL-1 alone by size exclusion chromatography (SEC; Superdex 75 HR 10/30 column, GE Healthcare), with 20 mM Hepes (pH 7.4) and 150 mM NaCl as equilibration buffer.

For isolation of Alphabody:HSA complexes, the Alphabody was expressed as described above. Subsequent to cell lysis, his-tagged Alphabody was captured by IMAC (5-ml HisTrap FF prepacked column, GE Healthcare) and polished by SEC (Superdex 75 HR 10/30 column, GE Healthcare). The complex with HSA (Sigma-Aldrich) was assembled and purified via SEC.

Crystal structure determination of the $_{\Delta N\Delta C}$MCL-1:CMPX-383B complex

$_{\Delta N\Delta C}$MCL-1:CMPX-383B was concentrated to 5.1 mg/ml. Commercial sparse matrix crystallization screens (Molecular Dimensions, Hampton Research, Jena Bioscience) were set up in a vapor-diffusion fashion, by mixing 100 nl of protein solution with 100 nl of mother liquor in SWISSCI 96-well triple drop plates. Plates were incubated at 294 K. After 6 months, crystals were detected under condition C7 of the JCSG-plus crystal screen (Jena Bioscience), containing 0.2 M zinc acetate dihydrate, 0.1 M sodium acetate (pH 4.5), and 10% (w/v) polyethylene glycol (PEG) 3000. These hits could be further optimized using gradient optimization in 96-well format and at different temperatures. Crystals diffracting x-rays to 2.3 Å were grown at 287 K under a condition containing 0.2 M zinc acetate dihydrate, 0.1 M sodium acetate (pH 5.5), and 2% PEG 3000. Before cryo-cooling by plunging into liquid nitrogen, these crystals were stepwise cryoprotected to contain a final concentration of 30% (v/v) PEG 400. Diffraction data were collected at 100 K at the ESRF ID23-2 beamline, Grenoble. Diffraction data were indexed, integrated, and scaled using the XDS Program Package (*75*). Initial phases were obtained using maximum-likelihood molecular replacement by Phaser from the CCP4 package (*76*, *77*) using the crystallographic model of MCL-1 as a search model [Protein Data Bank (PDB) code 3MK8] (*14*). Structure building and refinement were performed iteratively using COOT (*78*), PHENIX (*79*), BUSTER (*80*), and the PDB-REDO server (*81*). The Alphabody structure was built and chain-traced from scratch into the electron density.

Crystal structure determination of the HSA:CMPX-383B complex

Purified HSA:CMPX-383B complex was concentrated to 95 mg/ml. Crystallization screens containing 14 to 24% PEG 3350, 0.2 M ammonium phosphate, and 0.1 M acetate (pH 4.2 to pH 5.6), bis-tris (pH 5.8 to pH 7.0), or bis-tris propane (pH 7.0 to pH 9.0) buffer were set up in a vapor-diffusion fashion, by mixing 100 nl of protein solution with 100 nl of mother liquor in SWISSCI 96-well triple drop plates. Plates were incubated at 287, 294, or 310 K. Crystals with a plate-like morphology, diffracting x-rays to 3.27 Å, were grown at 310 K under a condition containing 18% (w/v) PEG 3350, 0.1 M bis-tris (pH 6.8), and 0.2 M ammonium phosphate. Before cryo-cooling by plunging into liquid nitrogen, these crystals were cryoprotected to contain a final concentration of 25% (w/v) PEG 3350 and 10% (v/v) glycerol. Diffraction data were collected at 100 K at the P14 microfocus beamline at PETRA III, Hamburg. Diffraction data were indexed, integrated, and scaled using the XDS Program Package (*75*). The resulted dataset was truncated and rescaled using the STARANISO anisotropy & Bayesian estimation server (*82*). Initial phases were obtained using maximum-likelihood molecular replacement by Phaser from the CCP4 package (*76*, *77*) using the crystallographic model of HSA as search model (PDB code 4Z69) (*83*). Structure building and refinement were performed iteratively using COOT (*78*), PHENIX (*79*), BUSTER (*80*), and the PDB-REDO server (*81*). The Alphabody structure was built and chain-traced from scratch into the electron density.

SUPPLEMENTARY MATERIALS

Supplementary material for this article is available at http://advances.sciencemag.org/cgi/content/full/7/13/eabe1682/DC1

View/request a protocol for this paper from *Bio-protocol*.

REFERENCES AND NOTES

1. A. L. Grilo, A. Mantalaris, The increasingly human and profitable monoclonal antibody market. *Trends Biotechnol.* **37**, 9–16 (2019).
2. L. Urquhart, Top drugs and companies by sales in 2018. *Nat. Rev. Drug Discov.* **18**, 245 (2019).
3. U.S. Food and Drug Administration, Center for Drug Evaluation and Research. CABLIVI (caplicizumab-yhdp) BLA approval letter, June 02, 2019. Retrieved Februari 25, 2021, from https://www.accessdata.fda.gov/drugsatfda_docs/appletter/2019/761112Orig1s000ltr.pdf.
4. S. Hober, S. Lindbo, J. Nilvebrant, Bispecific applications of non-immunoglobulin scaffold binders. *Methods* **154**, 143–152 (2019).
5. R. Vazquez-Lombardi, T. G. Phan, C. Zimmermann, D. Lowe, L. Jermutus, D. Christ, Challenges and opportunities for non-antibody scaffold drugs. *Drug Discov. Today* **20**, 1271–1283 (2015).
6. U. Binder, A. Skerra, in *Therapeutic Proteins: Strategies to Modulate Their Plasma Half-Lives*, 1-372 (Wiley, 2012).
7. J. Desmet, K. Verstraete, Y. Bloch, E. Lorent, Y. Wen, B. Devreese, K. Vandenbroucke, S. Loverix, T. Hettmann, S. Deroo, K. Somers, P. Henderikx, I. Lasters, S. N. Savvides, Structural basis of IL-23 antagonism by an Alphabody protein scaffold. *Nat. Commun.* **5**, 5237 (2014).
8. Y. Bloch, L. Bouchareychas, R. Merceron, K. Składanowska, L. Van den Bossche, S. Detry, S. Govindarajan, D. Elewaut, F. Haerynck, M. Dullaers, I. E. Adamopoulos, S. N. Savvides, Structural activation of pro-inflammatory human cytokine IL-23 by cognate IL-23 receptor enables recruitment of the shared receptor IL-12Rβ1. *Immunity* **48**, 45–58.e6 (2018).
9. C. T. Nguyen, Y. Bloch, K. Składanowska, S. N. Savvides, I. E. Adamopoulos, Pathophysiology and inhibition of IL-23 signaling in psoriatic arthritis: A molecular insight. *Clin. Immunol.* **206**, 15–22 (2019).
10. K. L. O'neill, K. Huang, J. Zhang, Y. Chen, X. Luo, Inactivation of prosurvival Bcl-2 proteins activates Bax/Bak through the outer mitochondrial membrane. *Genes Dev.* **30**, 973–988 (2016).
11. H. Kim, M. Rafiuddin-Shah, H. C. Tu, J. R. Jeffers, G. P. Zambetti, J. J. D. Hsieh, E. H. Y. Cheng, Hierarchical regulation of mitochondrion-dependent apoptosis by BCL-2 subfamilies. *Nat. Cell Biol.* **8**, 1348–1358 (2006).
12. E. H. Y. Cheng, M. C. Wei, S. Weiler, R. A. Flavell, T. W. Mak, T. Lindsten, S. J. Korsmeyer, BCL-2, BCL-XL sequester BH3 domain-only molecules preventing BAX- and BAK-mediated mitochondrial apoptosis. *Mol. Cell* **8**, 705–711 (2001).
13. M. Sattler, Structure of Bcl-xL-Bak peptide complex: Recognition between regulators of apoptosis. *Science* **275**, 983–986 (1997).
14. M. L. Stewart, E. Fire, A. E. Keating, L. D. Walensky, The MCL-1 BH3 helix is an exclusive MCL-1 inhibitor and apoptosis sensitizer. *Nat. Chem. Biol.* **6**, 595–601 (2010).
15. X. X. Cao, I. Mohuiddin, F. Ece, D. J. McConkey, W. R. Smythe, Histone deacetylase inhibitor downregulation of bcl-xl gene expression leads to apoptotic cell death in mesothelioma. *Am. J. Respir. Cell Mol. Biol.* **25**, 562–568 (2001).
16. A. Y. Bedikian, M. Millward, H. Pehamberger, R. Conry, M. Gore, U. Trefzer, A. C. Pavlick, R. DeConti, E. M. Hersh, P. Hersey, J. M. Kirkwood, F. G. Haluska, Bcl-2 antisense (oblimersen sodium) plus dacarbazine in patients with advanced melanoma: The oblimersen melanoma study group. *J. Clin. Oncol.* **24**, 4738–4745 (2006).
17. L. Gandhi, D. R. Camidge, M. R. De Oliveira, P. Bonomi, D. Gandara, D. Khaira, C. L. Hann, E. M. McKeegan, E. Litvinovich, P. M. Hemken, C. Dive, S. H. Enschede, C. Nolan, Y. L. Chiu, T. Busman, H. Xiong, A. P. Krivoshik, R. Humerickhouse, G. I. Shapiro, C. M. Rudin, Phase I study of navitoclax (ABT-263), a novel bcl-2 family inhibitor, in patients with small-cell lung cancer and other solid tumors. *J. Clin. Oncol.* **29**, 909–916 (2011).
18. F. Vaillant, D. Merino, L. Lee, K. Breslin, B. Pal, M. E. Ritchie, G. K. Smyth, M. Christie, L. J. Phillipson, C. J. Burns, G. B. Mann, J. E. Visvader, G. J. Lindeman, Targeting BCL-2 with the BH3 mimetic ABT-199 in estrogen receptor-positive breast cancer. *Cancer Cell* **24**, 120–129 (2013).
19. S. Kitada, I. M. Pedersen, A. D. Schimmer, J. C. Reed, Dysregulation of apoptosis genes in hematopoietic malignancies. *Oncogene* **21**, 3459–3474 (2002).
20. D. Hanahan, R. A. Weinberg, Hallmarks of cancer: The next generation. *Cell* **144**, 646–674 (2011).
21. D. Hanahan, R. A. Weinberg, The hallmarks of cancer. *Cell* **100**, 57–70 (2000).
22. I. Gojo, B. Zhang, R. G. Fenton, The cyclin-dependent kinase inhibitor flavopiridol induces apoptosis in multiple myeloma cells through transcriptional repression and down-regulation of Mcl-1. *Clin. Cancer Res.* **8**, 3527–3538 (2002).
23. J. Cidado, S. Boiko, T. Proia, D. Ferguson, S. W. Criscione, M. S. Martin, P. Pop-Damkov, N. Su, V. N. R. Franklin, C. S. R. Chilamakuri, C. S. D'Santos, W. Shao, J. C. Saeh, R. Koch, D. M. Weinstock, M. Zinda, S. E. Fawell, L. Drew, AZD4573 is a highly selective CDK9 inhibitor that suppresses Mcl-1 and induces apoptosis in hematologic cancer cells. *Clin. Cancer Res.* **26**, 922–934 (2020).
24. G. Wei, A. A. Margolin, L. Haery, E. Brown, L. Cucolo, B. Julian, S. Shehata, A. L. Kung, R. Beroukhim, T. R. Golub, Chemical genomics identifies small-molecule MCL1 repressors and BCL-xL as a predictor of MCL1 dependency. *Cancer Cell* **21**, 547–562 (2012).
25. M. E. S. Kahn, A. Senderowicz, E. A. Sausville, K. E. Barrett, Possible mechanisms of diarrheal side effects associated with the use of a novel chemotherapeutic agent, flavopiridol. *Clin. Cancer Res.* **7**, 343–349 (2001).
26. A. M. Senderowicz, Flavopiridol: The first cyclin-dependent kinase inhibitor in human clinical trials. *Investig. New Drugs* **17**, 313–320 (1999).
27. S. Boffo, A. Damato, L. Alfano, A. Giordano, CDK9 inhibitors in acute myeloid leukemia. *J. Exp. Clin. Cancer Res.* **37**, 36 (2018).
28. F. Morales, A. Giordano, Overview of CDK9 as a target in cancer research. *Cell Cycle* **15**, 519–527 (2016).
29. G. Brumatti, P. G. Ekert, Seeking a MCL-1 inhibitor. *Cell Death Differ.* **20**, 1440–1441 (2013).
30. S. Fletcher, MCL-1 inhibitors–where are we now (2019)? *Expert Opin. Ther. Pat.* **29**, 909–919 (2019).
31. L. Vela, I. Marzo, Bcl-2 family of proteins as drug targets for cancer chemotherapy: The long way of BH3 mimetics from bench to bedside. *Curr. Opin. Pharmacol.* **23**, 74–81 (2015).
32. M. H. Hecht, J. S. Richardson, D. C. Richardson, R. C. Ogden, Characterization of Felix : Four-helix bundle protein of native-like sequence. *Science* **249**, 884–891 (1988).
33. H. W. Hellinga, Rational protein design: Combining theory and experiment. *Proc. Natl. Acad. Sci. U.S.A.* **94**, 10015–10017 (1997).
34. F. Pucci, M. Rooman, Improved insights into protein thermal stability: From the molecular to the structurome scale. *Philos. Trans. R. Soc. A Math. Phys. Eng. Sci.* **374**, 20160141 (2016).
35. S. B. Fonseca, M. P. Pereira, S. O. Kelley, Recent advances in the use of cell-penetrating peptides for medical and biological applications. *Adv. Drug Deliv. Rev.* **61**, 953–964 (2009).
36. F. Madani, S. Lindberg, Ü. Langel, S. Futaki, A. Gräslund, Mechanisms of cellular uptake of cell-penetrating peptides. *J. Biophys.* **2011**, 1–10 (2011).
37. F. Wang, Y. Wang, X. Zhang, W. Zhang, S. Guo, F. Jin, Recent progress of cell-penetrating peptides as new carriers for intracellular cargo delivery. *J. Control. Release* **174**, 126–136 (2014).
38. Z. Qian, T. Liu, Y. Y. Liu, R. Briesewitz, A. M. Barrios, S. M. Jhiang, D. Pei, Efficient delivery of cyclic peptides into mammalian cells with short sequence motifs. *ACS Chem. Biol.* **8**, 423–431 (2012).

39. Z. Qian, J. R. Larochelle, B. Jiang, W. Lian, R. L. Hard, N. G. Selner, R. Luechapanichkul, A. M. Barrios, D. Pei, Early endosomal escape of a cyclic cell-penetrating peptide allows effective cytosolic cargo delivery. *Biochemistry* **53**, 4034–4046 (2014).
40. G. Guidotti, L. Brambilla, D. Rossi, Cell-penetrating peptides: From basic research to clinics. *Trends Pharmacol. Sci.* **38**, 406–424 (2017).
41. M. Ghandi, F. W. Huang, J. Jané-Valbuena, G. V. Kryukov, C. C. Lo, E. R. McDonald, J. Barretina, E. T. Gelfand, C. M. Bielski, H. Li, K. Hu, A. Y. Andreev-Drakhlin, J. Kim, J. M. Hess, B. J. Haas, F. Aguet, B. A. Weir, M. V. Rothberg, B. R. Paolella, M. S. Lawrence, R. Akbani, Y. Lu, H. L. Tiv, P. C. Gokhale, A. de Weck, A. A. Mansour, C. Oh, J. Shih, K. Hadi, Y. Rosen, J. Bistline, K. Venkatesan, A. Reddy, D. Sonkin, M. Liu, J. Lehar, J. M. Korn, D. A. Porter, M. D. Jones, J. Golji, G. Caponigro, J. E. Taylor, C. M. Dunning, A. L. Creech, A. C. Warren, J. M. McFarland, M. Zamanighomi, A. Kauffmann, N. Stransky, M. Imielinski, Y. E. Maruvka, A. D. Cherniack, A. Tsherniak, F. Vazquez, J. D. Jaffe, A. A. Lane, D. M. Weinstock, C. M. Johannessen, M. P. Morrissey, F. Stegmeier, R. Schlegel, W. C. Hahn, G. Getz, G. B. Mills, J. S. Boehm, T. R. Golub, L. A. Garraway, W. R. Sellers, Next-generation characterization of the Cancer Cell Line Encyclopedia. *Nature* **569**, 503–508 (2019).
42. J. Barretina, G. Caponigro, N. Stransky, K. Venkatesan, A. A. Margolin, S. Kim, C. J. Wilson, J. Lehár, G. V. Kryukov, D. Sonkin, A. Reddy, M. Liu, L. Murray, M. F. Berger, J. E. Monahan, P. Morais, J. Meltzer, A. Korejwa, J. Jané-Valbuena, F. A. Mapa, J. Thibault, E. Bric-Furlong, P. Raman, A. Shipway, I. H. Engels, J. Cheng, G. K. Yu, J. Yu, P. Aspesi, M. De Silva, K. Jagtap, M. D. Jones, L. Wang, C. Hatton, E. Palescandolo, S. Gupta, S. Mahan, C. Sougnez, R. C. Onofrio, T. Liefeld, L. MacConaill, W. Winckler, M. Reich, N. Li, J. P. Mesirov, S. B. Gabriel, G. Getz, K. Ardlie, V. Chan, V. E. Myer, B. L. Weber, J. Porter, M. Warmuth, P. Finan, J. L. Harris, M. Meyerson, T. R. Golub, M. P. Morrissey, W. R. Sellers, R. Schlegel, L. A. Garraway, The Cancer Cell Line Encyclopedia enables predictive modelling of anticancer drug sensitivity. *Nature* **483**, 603–607 (2012).
43. S. Lejon, I. M. Frick, L. Björck, M. Wikström, S. Svensson, Crystal structure and biological implications of a bacterial albumin binding module in complex with human serum albumin. *J. Biol. Chem.* **279**, 42924–42928 (2004).
44. A. L. Hopkins, C. R. Groom, The druggable genome. 1, 727–730 (2002).
45. L. W. Thomas, C. Lam, S. W. Edwards, Mcl-1; the molecular regulation of protein function. *FEBS Lett.* **584**, 2981–2989 (2010).
46. A. Ashkenazi, W. J. Fairbrother, J. D. Leverson, A. J. Souers, From basic apoptosis discoveries to advanced selective BCL-2 family inhibitors. *Nat. Rev. Drug Discov.* **16**, 273–284 (2017).
47. A. Kotschy, Z. Szlavik, J. Murray, J. Davidson, A. L. Maragno, G. Le Toumelin-Braizat, M. Chanrion, G. L. Kelly, J. N. Gong, D. M. Moujalled, A. Bruno, M. Csekei, A. Paczal, Z. B. Szabo, S. Sipos, G. Radics, A. Proszenyak, B. Balint, L. Ondi, G. Blasko, A. Robertson, A. Surgenor, P. Dokurno, I. Chen, N. Matassova, J. Smith, C. Pedder, C. Graham, A. Studeny, G. Lysiak-Auvity, A. M. Girard, F. Gravé, D. Segal, C. D. Riffkin, G. Pomilio, L. C. A. Galbraith, B. J. Aubrey, M. S. Brennan, M. J. Herold, C. Chang, G. Guasconi, N. Cauquil, F. Melchiore, N. Guigal-Stephan, B. Lockhart, F. Colland, J. A. Hickman, A. W. Roberts, D. C. S. Huang, A. H. Wei, A. Strasser, G. Lessene, O. Geneste, The MCL1 inhibitor S63845 is tolerable and effective in diverse cancer models. *Nature* **538**, 477–482 (2016).
48. J. Hoffmann, J. O. Wrabl, V. J. Hilser, The role of negative selection in protein evolution revealed through the energetics of the native state ensemble. *Proteins Struct. Funct. Bioinformatics* **84**, 435–447 (2016).
49. W. F. Degrado, C. M. Summa, V. Pavone, F. Nastri, A. Lombardi, De novo design and structural characterization of proteins and metalloproteins. *Annu. Rev. Biochem.* **68**, 779–819 (1999).
50. J. P. K. Doye, A. A. Louis, M. Vendruscolo, Inhibition of protein crystallization by evolutionary negative design. *Phys. Biol.* **1**, P9–P13 (2004).
51. R. R. Araghi, G. H. Bird, J. A. Ryan, J. M. Jenson, M. Godes, J. R. Pritz, R. A. Grant, A. Letai, L. D. Walensky, A. E. Keating, Iterative optimization yields Mcl-1–targeting stapled peptides with selective cytotoxicity to Mcl-1–dependent cancer cells. *Proc. Natl. Acad. Sci. U.S.A.* **115**, E886–E895 (2018).
52. K. Škrlec, B. Štrukelj, A. Berlec, Non-immunoglobulin scaffolds: A focus on their targets. *Trends Biotechnol.* **33**, 408–418 (2015).
53. C. Tiede, R. Bedford, S. J. Heseltine, G. Smith, I. Wijetunga, R. Ross, D. Alqallaf, A. P. E. Roberts, A. Balls, A. Curd, R. E. Hughes, H. Martin, S. R. Needham, L. C. Zanetti-Domingues, Y. Sadigh, T. P. Peacock, A. A. Tang, N. Gibson, H. Kyle, G. W. Platt, N. Ingram, T. Taylor, L. P. Coletta, I. Manfield, M. Knowles, S. Bell, F. Esteves, A. Maqbool, R. K. Prasad, M. Drinkhill, R. S. Bon, V. Patel, S. A. Goodchild, M. Martin-Fernandez, R. J. Owens, J. E. Nettleship, M. E. Webb, M. Harrison, J. D. Lippiat, S. Ponnambalam, M. Peckham, A. Smith, P. K. Ferrigno, M. Johnson, M. J. McPherson, D. C. Tomlinson, Affimer proteins are versatile and renewable affinity reagents. *eLife* **6**, e24903 (2017).
54. L. K. J. Stadler, D. C. Tomlinson, T. Lee, M. A. Knowles, P. Ko Ferrigno, The use of a neutral peptide aptamer scaffold to anchor BH3 peptides constitutes a viable approach to studying their function. *Cell Death Dis.* **5**, e1037 (2014).
55. V. J. Bruce, M. Lopez-Islas, B. R. McNaughton, Resurfaced cell-penetrating nanobodies: A potentially general scaffold for intracellularly targeted protein discovery. *Protein Sci.* **25**, 1129–1137 (2016).
56. E. G. Stanzl, B. M. Trantow, J. R. Vargas, P. A. Wender, Fifteen years of cell-penetrating, guanidinium-rich molecular transporters: Basic science, research tools, and clinical applications. *Acc. Chem. Res.* **45**, 2944–2954 (2013).
57. S. M. Fuchs, R. T. Raines, Arginine grafting to endow cell permeability. *ACS Chem. Biol.* **2**, 167–170 (2007).
58. D. B. Thompson, J. J. Cronican, D. R. Liu, Engineering and identifying supercharged proteins for macromolecule delivery into mammalian cells. *Methods Enzymol.* **503**, 293–319 (2012).
59. J. J. Cronican, K. T. Beier, T. N. Davis, J. C. Tseng, W. Li, D. B. Thompson, A. F. Shih, E. M. May, C. L. Cepko, A. L. Kung, Q. Zhou, D. R. Liu, A class of human proteins that deliver functional proteins into mammalian cells in vitro and in vivo. *Chem. Biol.* **18**, 833–838 (2011).
60. J. J. Cronican, D. B. Thompson, K. T. Beier, B. R. McNaughton, C. L. Cepko, D. R. Liu, Potent delivery of functional proteins into mammalian cells in vitro and in vivo using a supercharged protein. *JACS Chem. Biol.* **5**, 747–752 (2010).
61. J. Sadek, M. G. Wuo, D. Rooklin, A. Hauenstein, S. H. Hong, A. Gautam, H. Wu, Y. Zhang, E. Cesarman, P. S. Arora, Modulation of virus-induced NF-κB signaling by NEMO coiled coil mimics. *Nat. Commun.* **11**, 1786 (2020).
62. P. S. Huang, S. E. Boyken, D. Baker, The coming of age of de novo protein design. *Nature* **537**, 320–327 (2016).
63. B. Kuhlman, P. Bradley, Advances in protein structure prediction and design. *Nat. Rev. Mol. Cell Biol.* **20**, 681–697 (2019).
64. M. Gebauer, A. Skerra, Engineered protein scaffolds as next-generation therapeutics. *Annu. Rev. Pharmacol. Toxicol.* **60**, 391–415 (2020).
65. A. E. Tron, M. A. Belmonte, A. Adam, B. M. Aquila, L. H. Boise, E. Chiarparin, J. Cidado, K. J. Embrey, E. Gangl, F. D. Gibbons, G. P. Gregory, D. Hargreaves, J. A. Hendricks, J. W. Johannes, R. W. Johnstone, S. L. Kazmirski, J. G. Kettle, M. L. Lamb, S. M. Matulis, A. K. Nooka, M. J. Packer, B. Peng, P. B. Rawlins, D. W. Robbins, A. G. Schuller, N. Su, W. Yang, Q. Ye, X. Zheng, J. P. Secrist, E. A. Clark, D. M. Wilson, S. E. Fawell, A. W. Hird, Discovery of Mcl-1-specific inhibitor AZD5991 and preclinical activity in multiple myeloma and acute myeloid leukemia. *Nat. Commun.* **9**, 5341 (2018).
66. A. L. Maragno, P. Mistry, A. Kotschy, Z. Szlavik, J. Murray, J. Davidson, G. Le Toumelin-Braizat, M. Chanrion, A. Bruno, A. Claperon, H. Maacke, E. Morris, Y. Wang, A. Derreal, M. Csekei, A. Paczal, Z. Szabo, S. Sipos, A. Proszenyak, B. Balint, A. Surgenor, P. Dokurno, N. Matassova, I. Chen, G. Lysiak-Auvity, A.-M. Girard, F. Grave, F. Colland, E. Halilovic, O. Geneste, S64315 (MIK665) is a potent and selective Mcl1 inhibitor with strong antitumor activity across a diverse range of hematologic tumor models [abstract]. *Cancer Res.* **79**, 4482 (2019).
67. S. Caenepeel, S. P. Brown, B. Belmontes, G. Moody, K. S. Keegan, D. Chui, D. A. Whittington, X. Huang, L. Poppe, A. C. Cheng, M. Cardozo, J. Houze, Y. Li, B. Lucas, N. A. Paras, X. Wang, J. P. Taygerly, M. Vimolratana, M. Zancanella, L. Zhu, E. Cajulis, T. Osgood, J. Sun, L. Damon, R. K. Egan, P. Greninger, J. D. McClanaghan, J. Gong, D. Moujalled, G. Pomilio, P. Beltran, C. H. Benes, A. W. Roberts, D. C. Huang, A. Wei, J. Canon, A. Coxon, P. E. Hughes, AMG 176, a selective MCL1 inhibitor, is effective in hematologic cancer models alone and in combination with established therapies. *Cancer Discov.* **8**, 1582–1597 (2018).
68. M. Beck, A. Schmidt, J. Malmstroem, M. Claassen, A. Ori, A. Szymborska, F. Herzog, O. Rinner, J. Ellenberg, R. Aebersold, The quantitative proteome of a human cell line. *Mol. Syst. Biol.* **7**, 549 (2011).
69. A. Mateus, P. Matsson, P. Artursson, Rapid measurement of intracellular unbound drug concentrations. *Mol. Pharm.* **10**, 2467–2478 (2012).
70. Y. Phillip, G. Schreiber, Formation of protein complexes in crowded environments-from in vitro to in vivo. *FEBS Lett.* **587**, 1046–1052 (2013).
71. M. Sarkar, A. E. Smith, G. J. Pielak, Impact of reconstituted cytosol on protein stability. *Proc. Natl. Acad. Sci. U.S.A.* **110**, 19342–19347 (2013).
72. A. P. Minton, Quantitative assessment of the relative contributions of steric repulsion and chemical interactions to macromolecular crowding. *Biopolymers* **99**, 239–244 (2013).
73. H. X. Zhou, Influence of crowded cellular environments on protein folding, binding, and oligomerization: Biological consequences and potentials of atomistic modeling. *FEBS Lett.* **587**, 1053–1061 (2013).
74. M. M. Hann, G. L. Simpson, Intracellular drug concentration and disposition—The missing link? *Methods* **68**, 283–285 (2014).
75. W. Kabsch, Integration, scaling, space-group assignment and post-refinement. *Acta Crystallogr. Sect. D Biol. Crystallogr.* **66**, 133–144 (2010).
76. M. D. Winn, C. C. Ballard, K. D. Cowtan, E. J. Dodson, P. Emsley, P. R. Evans, R. M. Keegan, E. B. Krissinel, A. G. W. Leslie, A. McCoy, S. J. McNicholas, G. N. Murshudov, N. S. Pannu, E. A. Potterton, H. R. Powell, R. J. Read, A. Vagin, K. S. Wilson, Overview of the CCP4 suite and current developments. *Sect. D Biol. Crystallogr.* **67**, 235–242 (2011).
77. A. J. McCoy, R. W. Grosse-Kunstleve, P. D. Adams, M. D. Winn, L. C. Storoni, R. J. Read, Phaser crystallographic software. *J. Appl. Crystallogr.* **40**, 658–674 (2007).

78. P. Emsley, B. Lohkamp, W. G. Scott, K. Cowtan, Features and development of Coot. *Acta Crystallogr. Sect. D Biol. Crystallogr.* **66**, 486–501 (2010).
79. P. D. Adams, P. V. Afonine, G. Bunkóczi, V. B. Chen, I. W. Davis, N. Echols, J. J. Headd, L. W. Hung, G. J. Kapral, R. W. Grosse-Kunstleve, A. J. McCoy, N. W. Moriarty, R. Oeffner, R. J. Read, D. C. Richardson, J. S. Richardson, T. C. Terwilliger, P. H. Zwart, PHENIX: A comprehensive Python-based system for macromolecular structure solution. *Acta Crystallogr. Sect. D Biol. Crystallogr.* **66**, 213–221 (2010).
80. G. Bricogne, E. Blanc, M. Brandl, C. Flensbueg, P. Keller, W. Paciorek, P. Roversi, A. Sharff, O. S. Smart, C. Vonrhein, T. O. Womack, BUSTER version 2.10.3 (Global Phasing Ltd., 2011).
81. R. P. Joosten, F. Long, G. N. Murshudov, A. Perrakis, The PDB_REDO server for macromolecular structure model optimization. *IUCrJ* **1**, 213–220 (2014).
82. I. J. Tickle, C. Flensburg, P. Keller, W. Paciorek, A. Sharff, C. Vonrhein, G. Bricogne, STARANISO Global Phasing Ltd., Cambridge, UK (2018).
83. Y. Zhang, P. Lee, S. Liang, Z. Zhou, X. Wu, F. Yang, H. Liang, Structural basis of non-steroidal anti-inflammatory drug diclofenac binding to human serum albumin. *Chem. Biol. Drug Des.* **86**, 1178–1184 (2015).
84. B. Friguet, A. F. Chaffotte, L. Djavadi-Ohaniance, M. E. Goldberg, Measurements of the true affinity constant in solution of antigen-antibody complexes by enzyme-linked immunosorbent assay. *J. Immunol. Methods* **77**, 305–319 (1985).
85. Q. Liu, T. Moldoveanu, T. Sprules, E. Matta-Camacho, N. Mansur-Azzam, K. Gehring, Apoptotic regulation by MCL-1 through heterodimerization. *J. Biol. Chem.* **285**, 19615–19624 (2010).
86. S. Dutta, S. Gullá, T. S. Chen, E. Fire, R. A. Grant, A. E. Keating, Determinants of BH3 binding specificity for Mcl-1 versus Bcl-xL. *J. Mol. Biol.* **398**, 747–762 (2010).
87. E. Fire, S. V. Gullá, R. A. Grant, A. E. Keating, Mcl-1-Bim complexes accommodate surprising point mutations via minor structural changes. *Protein Sci.* **19**, 507–519 (2010).
88. P. E. Czabotar, E. F. Lee, G. V. Thompson, A. Z. Wardak, W. D. Fairlie, P. M. Colman, Mutation to bax beyond the BH3 domain disrupts interactions with pro-survival proteins and promotes apoptosis. *J. Biol. Chem.* **286**, 7123–7131 (2011).
89. E. F. Lee, P. E. Czabotar, H. Yang, B. E. Sleebs, G. Lessene, P. M. Colman, B. J. Smith, W. D. Fairlie, Conformational changes in Bcl-2 pro-survival proteins determine their capacity to bind ligands. *J. Biol. Chem.* **284**, 30508–30517 (2009).
90. A. Muppidi, K. Doi, S. Edwardraja, E. J. Drake, A. M. Gulick, H. G. Wang, Q. Lin, Rational design of proteolytically stable, cell-permeable peptide-based selective Mcl-1 inhibitors. *J. Am. Chem. Soc.* **134**, 14734–14737 (2012).
91. C. L. Day, C. Smits, F. C. Fan, E. F. Lee, W. D. Fairlie, M. G. Hinds, Structure of the BH3 domains from the p53-inducible BH3-only proteins Noxa and Puma in complex with Mcl-1. *J. Mol. Biol.* **380**, 958–971 (2008).
92. C. L. Day, L. Chen, S. J. Richardson, P. J. Harrison, D. C. S. Huang, M. G. Hinds, Solution structure of prosurvival Mcl-1 and characterization of its binding by proapoptotic BH3-only ligands. *J. Biol. Chem.* **280**, 4738–4744 (2005).

Acknowledgments: We thank the European Synchrotron Radiation Facility (Grenoble, France) and PETRA3/EMBL (Hamburg, Germany) for synchrotron beam time allocation and the staff of beamlines ID-23-1 (ESRF) and beamline P14 (EMBL-Hamburg) for technical support. **Funding:** This research was supported by the Flanders Agency for Innovation and Entrepreneurship (IWT Research and Development grant no. 120302), the Hercules Foundation (AUGE- 11-029), Research Foundation Flanders (grants G0E1516N and G0B4918N), Stand up to Cancer Program of the Flemish Cancer Society (Belgium), and Ghent University (grant no. BOF17-GOA-028). P.V.V. is supported by an ERC Starting Grant (no. 639784, EpiTALL). S.N.S. is a principal investigator at the Flanders Institute for Biotechnology (VIB). E.P. was supported by a predoctoral research fellowship from IWT-Flanders (Belgium). **Author contributions:** J.D., S.L., P.A., E.L., P.H., S.D., F.B., S.T., K.S., Y.M., and I.L. contributed to the design, characterization, and development of the Alphabody scaffold. E.L. carried out circular dichroism and stability experiments of Alphabodies. K.V. expressed and purified Alphabodies. M.V.T., T.P., L.R., and L.D. performed all Western blot analyses, expression analysis, flow cytometry experiments, and mouse xenograft experiments with contributions from P.V.V. M.V. contributed to the statistical analysis. E.P. expressed and purified recombinant proteins for structural studies, performed BLI measurements, and carried out structural studies of $_{\Delta N\Delta C}$MCL-1:CMPX-383B and HSA:CMPX-383B complexes with contributions from S.N.S. in data and structural analysis. I.L., P.V.V., and S.N.S. designed and supervised the study. E.P., M.V.T., and S.N.S. wrote the manuscript with contributions from all authors. **Competing interests:** J.D., S.L., K.V., P.A., P.H., and I.L. declare financial interests as employees of Complix N.V. (Ghent, Belgium), a biopharmaceutical company dedicated to the development of the Alphabody scaffold. S.D., J.D., I.L., and S.L. are inventors on a patent application EP2800759B1 related to this work filed by Complix N.V. (application no. 13701577.2, filing date: 4 January 2013, publication date: 18 July 2018). P.A., S.D., J.D., I.L., S.L., and K.S. are inventors on a patent application EP2909233B1 related to this work filed by Complix N.V. (application no. 13788700.6, filing date: 22 October 2013, publication date: 7 December 2016). The authors declare that they have no other competing interests. **Data and materials availability:** All data needed to evaluate the conclusions in the paper are present in the paper and the Supplementary Materials. Crystallographic coordinates and data have been deposited in the PDB (www.rcsb.org) with accession codes 6ZIE and 6ZL1. Additional data related to this paper may be requested from the authors.

Submitted 4 August 2020
Accepted 5 February 2021
Published 26 March 2021
10.1126/sciadv.abe1682

Citation: E. Pannecoucke, M. Van Trimpont, J. Desmet, T. Pieters, L. Reunes, L. Demoen, M. Vuylsteke, S. Loverix, K. Vandenbroucke, P. Alard, P. Henderikx, S. Deroo, F. Baatz, E. Lorent, S. Thiolloy, K. Somers, Y. McGrath, P. Van Vlierberghe, I. Lasters, S. N. Savvides, Cell-penetrating Alphabody protein scaffolds for intracellular drug targeting. *Sci. Adv.* **7**, eabe1682 (2021).

Science Advances

Cell-penetrating Alphabody protein scaffolds for intracellular drug targeting

Erwin Pannecoucke, Maaike Van Trimpont, Johan Desmet, Tim Pieters, Lindy Reunes, Lisa Demoen, Marnik Vuylsteke, Stefan Loverix, Karen Vandenbroucke, Philippe Alard, Paula Henderikx, Sabrina Deroo, Franky Baatz, Eric Lorent, Sophie Thiolloy, Klaartje Somers, Yvonne McGrath, Pieter Van Vlierberghe, Ignace Lasters and Savvas N. Savvides

Sci Adv **7** (13), eabe1682.
DOI: 10.1126/sciadv.abe1682